Trading oxygen for iron II. Oxygen- versus iron-dependent cosmic star formation history

M. Chruślińska^{1,2}, M. Curti¹, R. Pakmor², A. De Cia¹, J. Matthee³, A. Bhagwat², S. Monty^{4,5}

- European Southern Observatory, Karl-Schwarzschild-Str. 2, 85748 Garching, Germany
- Max Planck Institute for Astrophysics, Karl-Schwarzschild-Str. 1, D-85748 Garching, Germany
- Institute of Science and Technology Austria, Am Campus 1, 3400 Klosterneuburg, Austria
- Center for Interdisciplinary Exploration and Research in Astrophysics (CIERA), Northwestern University, 1800 Sherman Avenue,
- Department of Astronomy, New Mexico State University, Las Cruces, NM 88003, USA

ABSTRACT

Due to their different nucleosynthetic origin, a stellar population produces oxygen (O) and iron (Fe) on different timescales and their relative abundance can deviate strongly from solar. Galaxy formation models should treat these elements separately, as they play a distinct role in shaping physical phenomena. For example, oxygen mainly sets the gas cooling rate, while the iron abundance sets stellar atmosphere opacities impacting stellar evolution, spectra and feedback. Observations of star-forming galaxies usually only constrain gas-phase oxygen abundance, vastly limiting our capabilities of separating the cosmic evolution of oxygen and iron. Here, we present an observationally-motivated framework to scale the cosmic evolution of O and Fe abundances. We apply the relation between the α -enhancement and galaxies' specific star formation rate ([O/Fe]-sSFR; Chruslinska et al. 2024) to derive the Fe and O-dependent cosmic star-formation history (cSFH). We find that star formation with near-solar O/Fe is rare: at least 70% of the integrated cosmic stellar mass forms at non-solar O/Fe. The cosmic average metallicity is generally lower in [Fe/H] than in [O/H] (by up to a factor 3), with the offset increasing from z = 0 to redshifts $z \approx 3$ and then approaching the core-collapse O/Fe ratio. We validate our results against samples that probe the Fe-dependent cSFH in different regimes such as absorption-derived ([Fe/H]) from long gamma-ray bursts. Our results impact the interpretations of stellar and galaxy spectra and the predicted rates of transients, especially those linked to metal-poor progenitors (e.g., black hole mergers).

Key words. Stars: abundances, formation - Galaxies: abundances, evolution, star formation

2 Max Planck Institute for Astrophysics, Karl-Schwarzschild-Str.
3 Institute of Science and Technology Austria, Am Campus 1, 34d
4 Center for Interdisciplinary Exploration and Research in Astrop Evanston, IL 60201, USA
5 Department of Astronomy, New Mexico State University, Las C

Received November , 2025; accepted XX XX, 2025

Received November , 2025; accepted XX XX, 2025

ABST

Due to their different nucleosynthetic origin, a stellar population p relative abundance can deviate strongly from solar. Galaxy forma distinct role in shaping physical phenomena. For example, oxyge stellar atmosphere opacities impacting stellar evolution, spectra a constrain gas-phase oxygen abundance, vastly limiting our capabil we present an observationally-motivated framework to scale the between the α-enhancement and galaxies' specific star formation O-dependent cosmic star-formation history (cSFH). We find that integrated cosmic stellar mass forms at non-solar O/Fe. The cosm (by up to a factor 3), with the offset increasing from z = 0 to re We validate our results against samples that probe the Fe-depende from long gamma-ray bursts. Our results impact the interpretation: especially those linked to metal-poor progenitors (e.g., black hole properties of both stars (are in the surrounding medium. Increasing metallicity (abundance of elements heavier than helium) alters the physics and observable properties of both stars (Garcia et al. 2021; Eldridge & Stanway 2022; Vink 2022) and galaxies (Bromm & Loeb 2003; Maiolino & Mannucci 2019; Kewley et al. 2019), but not all elements affect evolution equally. Among them, oxygen and iron provide a striking example: they regulate different key processes and their abundances evolve on different timescales. Oxygen largely sets gas cooling, regulating how efficiently gas is converted into stars (Bromm & Loeb 2003; Richings et al. 2014; Katz et al. 2022; Sharda et al. 2023); iron-group elements control stellar opacities and radiation-driven winds (Iglesias & Rosers 1996; Vink et al. Sharda et al. 2023); iron-group elements control stellar opacities and radiation-driven winds (Iglesias & Rogers 1996; Vink et al. 2001), shaping stellar lives and deaths (Puls et al. 2008; Langer 2012; Smith 2014; Meynet et al. 2015; Heger et al. 2023), transient formation and properties (Langer & Norman 2006; Belczynski et al. 2010b; Perley et al. 2016; Schulze et al. 2018; Chruślińska et al. 2024a), ionizing-radiation output (e.g. Leitherer et al. 1999; Stanway & Eldridge 2018; Götberg et al. 2019, 2020), and feedback on galactic scales (Eldridge & Stanway 2022). Oxygen is produced by sources linked to massive stars and released promptly after star formation (Woosley et al. 2002; Heger et al. 2003; Janka et al. 2007; Schneider et al. 2021;

Kobayashi & Taylor 2023). Iron additionally has a substantial contribution from Type Ia supernovae (Tinsley 1979; Nomoto et al. 1997; Maoz et al. 2014; Kobayashi et al. 2020) with a wide delay-time distribution (Nomoto 1982; Iben & Tutukov 1984; Webbink 1984; Greggio 2005; Maoz & Mannucci 2012; Wang & Han 2012; Maoz et al. 2014; Livio & Mazzali 2018). Consequently, their relative abundance can depart from the solar ratio by a factor of ≥ 5 (Matteucci & Greggio 1986; Wheeler et al. 1989; Kobayashi & Taylor 2023; Chruślińska et al. 2024b; Monty et al. 2025). Observations of star-forming galaxies typically constrain only oxygen, which is the most abundant metal with strong emission lines (Maiolino & Mannucci 2019) available for growing samples across redshifts (Nakajima et al. 2023; Chemerynska et al. 2024; Curti et al. 2024; Revalski et al. 2024; Sanders et al. 2024). By contrast, the iron abundance in starforming gas is particularly difficult to determine (e.g. due to faint lines and strong dust depletion) and will likely remain unavailable for representative samples in the near term (Chruślińska et al. 2024b). Consequently, oxygen abundance is often used as a proxy for it, assuming a scaling that maintains relative abundance ratios as determined for the Sun. This can lead to important and as yet unaccounted for errors - here we propose a method to address this issue.

In Paper I, Chruślińska et al. (2024b) (Ch24) introduced the relation between oxygen-to-iron abundance ratio and the specific star formation rate of galaxies ([O/Fe] - sSFR relation) as an effective to translate oxygen to iron abundances. Ch24 showed that the relation is supported by cosmological simulations and basic theoretical expectations, and used a homogenised sample of star-forming galaxies to provide empirical constraints. Here we apply this relation to infer the iron-dependent cosmic star formation history, $f_{SFR}(Z_{Fe/H}, t)$, and compare it with its oxygen-based counterpart, $f_{SFR}(Z_{O/H}, t)$. To this end, we expand and update the framework developed in Chruślińska & Nelemans (2019) (ChN19) and Chruślińska et al. (2021) (Ch21), which estimates $f_{SFR}(Z_{O/H}, t)$ by combining empirical distributions of galaxy properties (star formation rate SFR, gas-phase oxygen abundance $Z_{O/H}$, stellar mass M_*) with number statistics, while propagating the associated uncertainties. As a verification step, we compare our $f_{SFR}(Z_{Fe/H}, t)$ predictions with samples of Milky Way globular clusters (Carretta et al. 2009; VandenBerg et al. 2013) and RR Lyrae stars in local dwarfs (Bellazzini et al. 2025), which probe different parts of the cosmic star formation rate (SFRD) distribution in iron (Sec. 3.1). In Sec. 6 we further compare our results with the absorption-based cosmic SFRDweighted average metallicity probed by long gamma-ray bursts (LGRBs; Heintz et al. 2023).

Where appropriate, we adopt a standard flat cosmology with Ω_{M} = 0.3, Ω_{Λ} = 0.7, and H_0 = 70 km s⁻¹ Mpc⁻¹ (Hinshaw et al. 2013) and assume a Kroupa (2001) initial mass function (IMF). The terms 'redshift' (z), 'cosmic time' (t) and 'lookback time' are used interchangeably throughout the paper (z= lookback time = 0 at present day), the relation between them is fixed within the assumed cosmological model. We use the solar reference abundances from Grevesse & Sauval (1998) for consistency with previous work $(12+\log_{10}(O/H)_{\odot}=8.83, 12+\log_{10}(Fe/H)_{\odot}=7.5,$ log₁₀(O/Fe)_⊙=1.33). Where necessary, we shift abundances of literature samples to this solar reference scale. Different solar reference values are reported and used across the literature (especially for oxygen different estimates differ by ~0.15dex, e.g. Lodders et al. 2009; Asplund et al. 2009, 2021). This choice only affects the numerical results reported for abundances relative to solar. Where these results cannot be straightforwardly converted to a different solar reference, we comment on the impact this has. We use the following notation to distinguish absolute abundances: $Z_{X/H}=12+\log_{10}(X/H)$ and abundances relative to solar: $[X/H] = Z_{X/H} - Z_{X/H;\odot}$, where the index 'X=O' for oxygen and 'X=Fe' for iron, respectively.

2. Method: trading oxygen for iron using the [O/Fe] - sSFR relation of galaxies

We aim to self-consistently derive and compare the oxygen-based $f_{SFR}(Z_{O/H},t)$ and iron-based $f_{SFR}(Z_{Fe/H},t)$. We follow the phenomenological approach detailed in ChN19 and Ch21. The key additional step introduced in this work is the application of the [O/Fe] – sSFR relation of galaxies from Ch24, which allows us to estimate $f_{SFR}(Z_{Fe/H},t)$. The core idea of our framework is summarized below. Our approach requires knowledge of the following main ingredients:

- 1) [O/Fe] specific SFR relation (redshift invariant)
- 2) Distribution of sSFR of galaxies as a function of redshift
- 3) (a) Distribution of $Z_{O/H}$ of galaxies
 - (b) Relation linking galaxy $Z_{O/H}$ and sSFR
 - (c) Evolution of (3a) and potentially (3b) with redshift
- 4) Number density of galaxies n_{gal} with different sSFR and $Z_{O/H}$ as a function of redshift

In ChN19 and Ch21, (2-4) are determined based on a compilation of observational studies and extrapolated where necessary. (2) and (3a) are characterized as a function of the galaxy's stellar mass M_* . At a fixed z, galaxies follow a ridge in the $Z_{O/H}$ - $\log_{10}(M_*)$ plane with characteristic scatter σ_{MZR} in $Z_{O/H}$, referred to as the mass-metallicity relation (MZR, e.g. Tremonti et al. 2004; Maiolino et al. 2008; Curti et al. 2020; Sanders et al. 2021; Nakajima et al. 2023; Curti et al. 2024; Scholte et al. 2024, see the review by Maiolino & Mannucci 2019). We obtain the distribution of sSFR (2) starting from the distribution of galaxies observed in the $\log_{10}(SFR)$ - $\log_{10}(M_*)$ plane. The main ridge in this plane defines the galaxy main sequence (e.g. Brinchmann et al. 2004; Speagle et al. 2014; Tomczak et al. 2016; Popesso et al. 2023; Simmonds et al. 2025; Di Cesare et al. 2025, here called the star formation-mass relation - SFMR, for consistency with earlier work) with characteristic scatter σ_{SFR} . A bimodality in the $\log_{10}(SFR)$ - $\log_{10}(M_*)$ plane is sometimes observed, with the secondary ridge occupied by starburst (SB) galaxies and referred to as the SB sequence (e.g. Rodighiero et al. 2011; Sargent et al. 2012; Schreiber et al. 2015; Caputi et al. 2017; Rinaldi et al. 2025). If $Z_{O/H}$ and SFR (sSFR) were not correlated, these galaxy properties could be easily connected via M_* . In general this is not the case, and additional relation linking $Z_{O/H}$, SFR and M_* (3b) takes into account the observed anticorrelation between the galaxy's $Z_{O/H}$ and sSFR (called fundamental metallicity relation - FMR, e.g. Ellison et al. 2008; Mannucci et al. 2010, 2011; Yates et al. 2012; Andrews & Martini 2013; Lara-López et al. 2010; Sanders et al. 2018; Curti et al. 2020). FMR is found to be z-invariant in the models/simulations (Davé et al. 2011; Lagos et al. 2016; De Rossi et al. 2017; Torrey et al. 2018 but see Garcia et al. 2024) and is consistent with no evolution according to observations (e.g. Cresci et al. 2019; Sanders et al. 2021) at least up to z~3. If the FMR is z-invariant, (3c) the evolution of galaxy $Z_{O/H}$ with z is determined by the evolution of other galaxy properties. However, recent works obtain conflicting results regarding the FMR and its universality in the early Universe (e.g. Heintz et al. 2023; Langeroodi & Hjorth 2023; Nakajima et al. 2023; Curti et al. 2023, 2024, identify z≥6 galaxies showing significant departures from the z=0 FMR) and at low $M_* \lesssim 10^9 M_{\odot}$ (Kotiwale et al. 2025; Laseter et al. 2025). We note that $Z_{O/H}$ at z≥3 (and 3c) were essentially unconstrained prior to JWST, and the works of ChN19; Ch21 rely on different extrapolations in this regime. In Section 2.2 we review our assumptions in light of these new observational results and rule out some of those extrapolations, making a crucial update to our framework. Once (2) and (3) are fixed, the $Z_{Fe/H}$ of each galaxy (characterized by z, M_* , $Z_{O/H}$ and SFR) can be estimated using (1) (see Sec. 2.1). Following ChN19, to account for the fact that star formation within a galaxy occurs over a range of metallicities, we distribute the SFR in metallicity as a Gaussian centered on the $Z_{O/H}$ and $Z_{Fe/H}$ values assigned from the scaling relations. For simplicity, we adopt a common dispersion, $\sigma_{\nabla O/H} = \sigma_{\nabla Fe/H} = 0.14$ dex. The role of step (4) is to provide

(1) (see Sec. 2.1). Following ChN19, to account for the fact that star formation within a galaxy occurs over a range of metallicities, we distribute the SFR in metallicity as a Gaussian centered on the $Z_{\rm O/H}$ and $Z_{\rm Fe/H}$ values assigned from the scaling relations. For simplicity, we adopt a common dispersion, $\sigma_{\rm VO/H} = \sigma_{\rm VFe/H} = 0.14$ dex. The role of step (4) is to provide the 'weighting factor', i.e. account for the fact that galaxies with different properties are not equally abundant in the cosmic volume when counting their contribution to the cosmic star formation budget. All relevant galaxy properties in our framework can be linked via M_* , and the weighting $n_{gal}(M_*,z)$ is obtained from the galaxy stellar mass function (GSMF, e.g. Baldry et al. 2012; Muzzin et al. 2013; Stefanon et al. 2021). The product of (2) and (4) integrated over the full relevant range of M_* gives the total (i.e. at all metallicities) star formation rate density (SFRD). The result of this integration as a function of z gives the cosmic

star formation history (cSFH, section 5.1). By summing only the contribution of galaxies with a given $Z_{O/H}$ or $Z_{Fe/H}$, we derive the SFRD as a function of metallicity, i.e. either oxygenor iron-based metallicity-dependent cSFH.

For our initial estimate we assume:

- (1) [O/Fe] sSFR relation corresponding to the "mixed" Fe enrichment variation defined in Sec. 2.1
- (2) SFMR from Popesso et al. (2023) (P23), based on a homogenized set of observational literature estimates spanning 0 < z < 6, but with additional evolution in the normalisation at high z. This modification is motivated by the recent results of Simmonds et al. (2025), constraining the SFMR up to $z \sim 9$. Table C.1 (row " $a_{\rm SFR}=I+\ evol.$ ") provides implementation details. We include a small fraction of SB ($f_{\rm SB}=3\%$, as in Boco et al. 2021,Ch21), which yields negligible SB contribution to the cSFH.
- (3a) MZR(z=0) matching Curti et al. (2020) with the asymptotic value at high M_* ($Z_{O/H;MZR0}$) shifted by +0.2 dex (see Tab. C.1 for details). Ch24 show that such systematic shift in $Z_{O/H}$ estimated from electron temperature-sensitive auroral lines (and the derived strong line calibrations, including Curti et al. 2020) may be necessary to reconcile the average [O/Fe] of young star-forming galaxies and old Milky Way (MW) stars.
- (3b) FMR as described in Ch21, determined by MZR(z=0), SFMR(z=0) and a parameter $\nabla_{\rm FMR0}$, characterising the strength of the $Z_{O/H}$ SFR correlation at high SFR and low/intermediate M_*^{-1} . We use $\nabla_{\rm FMR0}=0.27$ as in Ch21.
- (3c) Fixed FMR at $z \le 3$, and the FMR with decreasing normalisation at z > 3 as discussed in Sec 2.2. This takes into account the potential additional $Z_{O/H}$ evolution beyond that resulting from a z-invariant FMR, as allowed by current observational constraints.
- (4) GSMF from ChN19 extrapolated to low $M_*=10^6 M_{\odot}$ with a z-dependent slope $\alpha_{\rm GSMF}(z)$ and updated to include more recent results, as described in Appendix A.

We refer to the model characterised by the above choices (1–4) as the 'example variation'. We use it in Section 3 to discuss the main characteristics of our results and show it in more detail. In Sec. 4 and beyond, we also explore alternative assumptions to assess the sensitivity of our results to these choices. The variations, summarized in Table C.1 in Appendix C, are selected to capture the major uncertainties in our framework while remaining broadly consistent with current constraints on the [O/Fe] – sSFR relation (Sec. 2.1), MZR (Sec. 2.2), and cSFH (Sec. 5.1).

2.1. The relation between [O/Fe] - specific SFR

Figure 1 summarizes constraints on the [O/Fe] - sSFR relation derived by Ch24, who also show that most of current theoretical expectations are consistent with these constraints. The gray boxes in Fig. 1 show the [O/Fe] in $\log_{10}(\text{sSFR})$ bins (spanning 0.13 - 99.87 percentiles of the mean). These were obtained after correcting the $Z_{O/H}$ and $Z_{Fe/H}$ of star-forming galaxies compiled from the literature for average systematic offsets (putting them on a 'common baseline'). Ch24 define several common baseline choices. We only show those for which the high sSFR 'plateau' of the [O/Fe]–sSFR relation is at the value consistent with the average <[O/Fe]>_{MW} of old metal-poor MW stars. These values are expected to be similar, reflecting a regime in which chemical

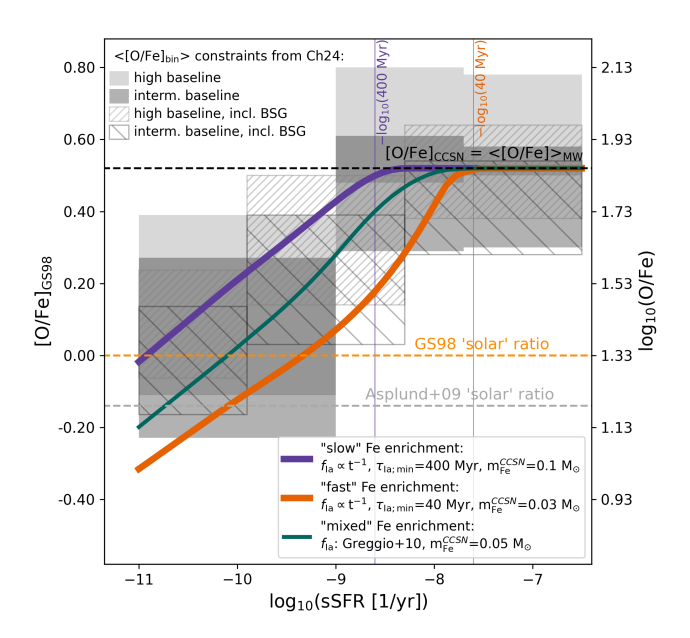


Fig. 1. The [O/Fe] - sSFR relation of galaxies. Colored lines show three model variations considered in this paper (purple - "slow" Fe enrichment, orange - "fast" Fe enrichment and green - "mixed" Fe enrichment), which span the range allowed by observational constraints discussed in Ch24 and shown as solid/hatched areas (see text for the details). The horizontal black line indicates the average abundance ratio of the Milky Way thick disc/halo dwarf stars with [Fe/H] <−2 from Amarsi et al. (2019). The horizontal orange line indicates our reference solar log₁₀(O/Fe)|_☉=1.33 dex (Grevesse & Sauval 1998). The zero point on the Asplund et al. (2009) solar scale is shown as a gray dashed line.

enrichment is dominated by core-collapse supernovae (CCSNe) from massive star progenitors that eject material with supersolar O/Fe. Hatched boxes show (tighter) constraints derived assuming that blue supergiant (BSG)-based metallicity (Bresolin et al. 2016, 2022) can be used as a measure of galaxy's $Z_{Fe/H}$. The colored lines in Fig. 1 show three model variations of the [O/Fe] - sSFR relation that span these constraints and which we consider here. These model relations are calculated following eq. 1 from Ch24, recalled below:

 $[O/Fe] = [O/Fe]_{CCSN}$

$$-\log_{10}\!\left(1+\frac{m_{Fe}^{Ia}}{m_{Fe}^{CCSN}}\frac{N_{Ia0}}{k_{CCSN}}\frac{\int_{0}^{t}SFR(t')f_{Ia}(t-t')\,dt'}{SFR}\right) \ \ \, (1$$

where $[O/Fe]_{CCSN}$ is the average core collapse supernova (CCSN) oxygen to iron abundance ratio relative to solar, m_{Fe}^{CCSN} and m_{Fe}^{Ia} is the average iron mass ejected per CCSN or SN Ia event, respectively, k_{CCSN} is the CCSN formation efficiency (i.e. number of CCSN formed per unit stellar mass formed), N_{Ia0} is the SN Ia formation efficiency (i.e. the Hubble time-integrated number of SN Ia formed per unit stellar mass) and f_{Ia} describes the SN Ia delay time distribution (DTD) normalised to unity when integrated over the Hubble time. For a fixed f_{Ia} , the relative iron production rate in SN Ia and CCSN $C_{Ia/CC} := \frac{m_{Fe}^{Ia}}{m_{Fc}^{CCSN}} \frac{N_{Ia0}}{k_{CCSN}}$ sets the slope of the relation, where m_{Fe}^{CCSN} appears to be the most uncertain factor ($C_{Ia/CC} \approx 0.074/m_{Fe}^{CCSN}$).

Following Ch24, we fix [O/Fe]_{CCSN}=<[O/Fe]>_{MW}=0.52 dex to match average abundance ratio of metal-poor MW stars from (Amarsi et al. 2019, used as a baseline for their careful treatment

¹ δ MZR = $-\nabla_{FMR0} \cdot \delta$ SFMR, where δ MZR and δ SFMR are the galaxy's offsets from the respective relations.

of non-LTE effects)². For the purpose of this work, we assume a power-law SN Ia DTD ($f_{Ia} \propto t^{-\alpha_{Ia}}$ at t> $\tau_{Ia;min}$ and zero at t< $\tau_{Ia;min}$) with $\alpha_{Ia}=1$. This particular choice does not affect our conclusions (other f_{Ia} parametrisations are possible, but they degenerate into [O/Fe]-sSFR relations, see examples in Ch24). What is important, however, is the uncertain turning point of the relation, which for the assumed DTD is set by the minimum SN Ia delay $\tau_{Ia;min}$ (thin vertical lines in Fig. 1). Therefore, we define two variations:

- (i) 'Fast' Fe enrichment: $\tau_{\rm Ia;min}$ =40 Myr and m^{CCSN}_{Fe}=0.03 M_{\odot} (or C_{Ia/CC}=2.5)
- (ii) 'Slow' Fe enrichment: $\tau_{\text{Ia;min}}$ =400 Myr and m_{Fe}^{CCSN}=0.1 M_{\odot} (or C_{Ia/CC}=0.74)

Those choices can be considered extreme based on current theoretical expectations (see sec. 5 in Ch24 and references therein) and until tighter constraints are available, we use (i) and (ii) to bracket the uncertainty in the [O/Fe]-sSFR relation. Additionally, we consider an intermediate scenario:

(iii) 'Mixed' Fe enrichment: f_{Ia} from Kashino et al. (2022) and m_{Fe}^{CCSN} =0.05 M_{\odot} (or $C_{Ia/CC}$ =1.48)

where the f_{Ia} is based on an analytic theoretical model from Greggio (2005, 2010) which allows for a mixed contribution of different proposed SN Ia progenitors.

2.2. $Z_{O/H}$ at high z: our model in light of JWST

The high z > 3 regime has only recently become accessible to empirical $Z_{O/H}$ studies, with the launch of the JWST enabling the detection of the emission lines conventionally used to determine the gas-phase metallicity. Here we take advantage of these new constraints to update our framework and validate assumptions about the $Z_{O/H}$ evolution made in ChN19 (MZR with a strong z dependence) and Ch21 (z-invariant FMR). These two approaches give consistent $f_{SFR}(Z_{O/H}, z)$ up to $z \le 3$, but lead to vastly different outcomes at higher z (Boco et al. 2021,Ch21). We model the evolution of the MZR assuming that the FMR is z-invariant and compare it with the recent z > 3 observational samples (Nakajima et al. 2023; Curti et al. 2024; Chemerynska et al. 2024) in Figure 2. We follow the phenomenological description of the FMR developed in Ch21, where the FMR is determined by the local MZR(z = 0) and SFMR(z = 0) relations and a single parameter ∇_{FMR0} . This approach captures the systematic differences in the FMR introduced by $Z_{O/H}$ and SFR determination methods (e.g. Kewley & Ellison 2008; Yates et al. 2012; Kashino et al. 2016; Telford et al. 2016; Maiolino & Mannucci 2019). MZR(z) shown in Fig. 2 as solid lines correspond to maximum density regions occupied by our model galaxies in the $Z_{O/H}$ - $log_{10}(M_*)$ plane at fixed z. This locus changes with z due to evolution of both SFMR and GSMF. We assume the MZR(z = 0) from Curti et al. (2020) (yellow solid line), SMFR and GSMF as described in Sec. 2^{3} .

The resulting MZR shows a strong evolution up to $z \approx 1.5$ (in the last ≈ 9.5 Gyr), by which point the average $Z_{O/H}$ of $\log(M_*/M_\odot) \lesssim 9$ galaxies decrease by ≈ 0.3 dex. This is broadly consistent with observational estimates, showing that the average $Z_{O/H}$ of galaxies at $z \approx 1-3$ are lower than estimated from z = 0 MZR by about 0.3 dex (e.g. Sanders et al. 2020; Topping et al. 2020; Cullen et al. 2021; Henry et al. 2021; Revalski et al.

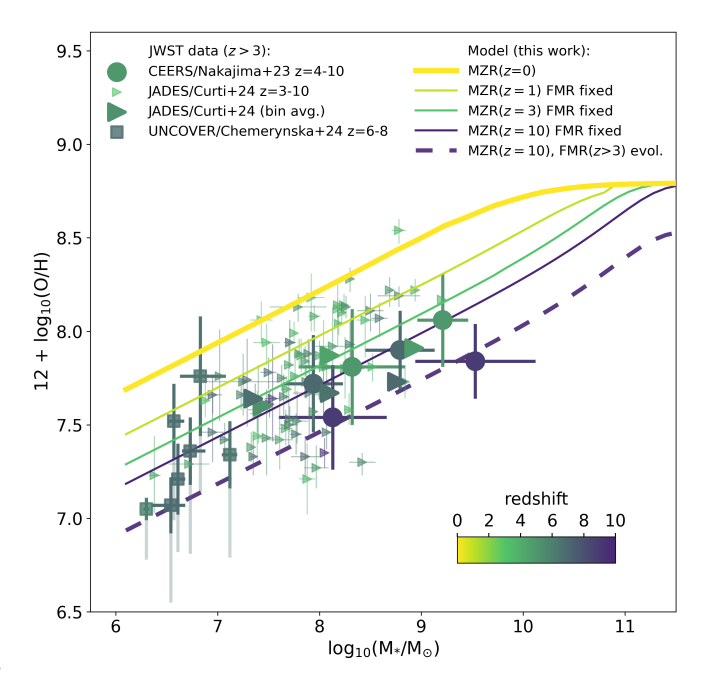


Fig. 2. Evolution of the gas-phase $Z_{O/H}$ -MZR in our model against z>3 data. MZR(z>3) predicted based on the known evolution of the SFMR and z-invariant FMR (modelled as in Ch21) is consistent with the current data, but additional evolution may be present. Solid lines - MZR at z=0, 1,3 10 assuming a z-invariant FMR. Dashed line - MZR at z=10, assuming additional evolution in the FMR normalization at z>3. Data points - z>3 samples from Nakajima et al. (2023) (circles, z-bin average), Curti et al. (2024) (triangles, small - individual, big - z-bin average) and Chemerynska et al. (2024) (squares, assuming calibration from Nakajima et al. (2022), faint errors extend to values estimated using Sanders et al. (2024) calibration). Data points are shown in blue for z<6.5 and in black for z>=6.5. Shown for a variation described in Sec. 2, but for MZR(z=0) from Curti et al. (2020) (i.e. without +0.2 dex offset, to compare with the data as reported).

2024; Stanton et al. 2024). Evolution within z = 1–3 range is difficult to quantify empirically as it is comparable to measurement uncertainties (e.g. Henry et al. 2021) and smaller than systematics (e.g. Laseter et al. 2024; Stanton et al. 2024) introduced by different high-z strong line metallicity calibrations used in the literature (e.g. Bian et al. 2018; Curti et al. 2020; Nakajima et al. 2023; Sanders et al. 2024)

At z > 3, the MZR in our universal FMR model decreases further by ≈ 0.2 dex by $z \approx 6$ and shows little evolution beyond this point. Observationally, the exact evolution of the MZR between z = 3–10 is currently unclear. Curti et al. (2024) analyse a sample of z = 3-10 galaxies from JADES (Bunker et al. 2023) and CEERS (Finkelstein et al. 2023) surveys, finding ~ 0.05 dex -0.25 dex offset with respect to $z \sim 3$ MZR (depending on the reference z = 3 relation). This is consistent with Nakajima et al. (2023), who point out lower average $Z_{O/H}$ in their z = 8–10 bin, but consistent with no MZR evolution between z = 4–10 within errors. Both Nakajima et al. (2023) and Curti et al. (2024) find weaker $Z_{O/H}$ evolution at the low M_* end. However, this has been challenged by Chemerynska et al. (2024) who analysed the low M_* galaxy sample from the UNCOVER survey (Bezanson et al. 2024).

The picture emerging from current observations is that the normalisation of the MZR at z = 3-10 is somewhere $\approx 0.4-0.7$ dex below that of the z = 0 relation (Curti et al. 2024; Nakajima

 $[\]overline{\ }^2$ Our results in terms of $Z_{Fe/H}$ and O/Fe values can simply be shifted by a constant to match other choices

³ MZR evolution is similar for all variations considered here, but see Ch21 and Fig. A4 therein for dependence on the MZR(z=0) and ∇ _{FMR0}.

et al. 2023; Morishita et al. 2024). Even with this uncertainty, it is clear that the extrapolation used in ChN19, leading to >1 dex decrease in $Z_{O/H}$ between z=3 and z=10, severely underestimates galaxy $Z_{O/H}$ at high z. In turn, the z-invariant FMR from Ch21 to MZR(z) which is broadly consistent with current observational estimates up to z=10. However, stronger evolution is also allowed within current uncertainties (i.e., the universal FMR may lead to overestimated $Z_{O/H}$ at z>6). To account for this possibility, we introduce a variation of our model in which the FMR normalisation decreases by 0.25 dex between z=3 and z=10. For simplicity, we assume that this decrease is linear with z (see Tab. C.1). The resulting MZR(z=10) is shown in Fig. 2 as a dashed line.

3. Iron-dependent cosmic star formation history: example variation

We begin the discussion of our results by highlighting the key differences between iron- and oxygen-based metallicity-dependent cSFH. Figure 3 shows the $f_{SFR}(Z_{Fe/H},z)$ (plotted as a 2-dimensional histogram in the [Fe/H] - z plane, colored by the SFRD) for our example variation described in Section 2. The corresponding $f_{SFR}(Z_{O/H},z)$ is shown in Fig. G.1. To compare the iron- and oxygen-based results, we plot the SFRD-weighted averages of [Fe/H] and [O/H] at each z (solid lines: \langle [Fe/H] \rangle SFRD - brown; \langle [O/H] \rangle SFRD - black). We note that:

- (i) The SFRD-weighted average metallicity is lower when iron is used as a metallicity probe instead of the oxygen, reflecting the delay in iron enrichment relative to oxygen. Relatedly, the distribution $f_{SFR}(Z_{Fe/H}, z)$ extends to lower metallicities than $f_{SFR}(Z_{O/H}, z)$. In Sec. 4 we show that their offset is sensitive primarily to the [O/Fe] sSFR relation.
- (ii) The offset between the $\langle [Fe/H] \rangle_{SFRD}$ and $\langle [O/H] \rangle_{SFRD}$ increases with z until $z \approx 3$ where $\langle [Fe/H] \rangle_{SFRD}$ shows a steeper evolution. At z > 3 this offset approaches a constant value. This is a consequence of the weak evolution of galaxies' sSFRs at $z \gtrsim 3$, and thus, their locations in the [O/Fe] sSFR plane.
- (iii) The mismatch between the two distributions suggests that the star formation with a solar O/Fe abundance ratio is rare throughout cosmic history (see Fig. G.2, showing the corresponding [O/Fe]-dependent cosmic SFH).

We further quantify point (iii) in Section 4.

3.1. Cross-check with observational samples

While the $f_{SFR}(Z_{O/H},z)$ is obtained by combining the empirical properties of galaxy populations across z, the $f_{SFR}(Z_{Fe/H},z)$ is inferred more indirectly. The $Z_{Fe/H}$ of young stars/gas is estimated from the galaxy's $Z_{O/H}$ and sSFR via the [O/Fe]–sSFR relation. To assess whether our results fall within a reasonable range, we compare them against three reference observational samples that probe different regions of $f_{SFR}(Z_{Fe/H},z)$, as discussed below and shown in Fig. 3.

3.1.1. RR Lyrae: [Fe/H] in low-mass, high-z galaxies

RR Lyrae are pulsating stars with typical ages of $\gtrsim 10$ Gyr, reaching $\gtrsim 12.5$ Gyr in GCs and in the lowest-mass dwarf galaxies (Catelan 2004, 2009; Sesar et al. 2014). They trace the properties of the oldest stellar populations. Following Bellazzini et al. (2025), we adopt the mean metallicity of RR Lyrae stars in local

dwarf galaxies ($\langle [Fe/H] \rangle_{RRLyr}$) as a proxy for the iron enrichment of the lowest-mass galaxies ($M_* < 10^8 \, M_\odot$) at $z \gtrsim 2-5$ (lookback times $\gtrsim 10$ - 12.5 Gyr). Specifically, we use the values listed in Table A.1 of Bellazzini et al. (2025), based on [Fe/H] estimates from Muraveva et al. (2025). These were derived from the pulsation periods and Fourier decomposition parameters of RR Lyrae light curves in Gaia Data Release 3 (Clementini et al. 2023).

As a minimum requirement, any viable model must reproduce the formation of stars with $\langle [\text{Fe/H}] \rangle_{\text{RRLyr}}$ at $z \gtrsim 2$, in the regime where galaxies with $M_* < 10^8 \, M_\odot$ contribute to $f_{\text{SFR}}(Z_{\text{Fe/H}}, z)$. Fig. 3 shows that this is the case, and that the full extent of the low [Fe/H]-high z tail of the $f_{\text{SFR}}(Z_{\text{Fe/H}}, z)$ probed by RR Lyrae can only be populated by star formation in $M_* < 10^8 M_\odot$ galaxies. Conversely, not accounting for such galaxies leads to negligible star formation at [Fe/H]<-2 at any z covered by our models.

3.1.2. MW globular clusters: [Fe/H] at high SFRD

Globular clusters (GCs) are old stellar systems, each thought to have formed in a brief star formation episode. While they host multiple stellar populations distinguished by variations in their light-element abundances, they generally exhibit only small spreads in $Z_{Fe/H}$, likely reflecting the iron content of the interstellar medium at the time of their formation (McKenzie & Bekki 2021; Legnardi et al. 2022; Monty et al. 2023; Legnardi et al. 2024). Both observations (e.g. Adamo et al. 2020a,b) and theory (e.g. Grudić et al. 2021) indicate that GC progenitor formation efficiency depends on the star-forming environment. Dense and most actively star-forming regions (such as found in local starbursts or in the early Universe) favor the formation of massive, long-lived clusters that can evolve into today's GCs (Adamo et al. 2020b; Reina-Campos et al. 2022; Kruijssen 2025) Thus, we expect the GCs to preferentially probe the regions of $f_{SFR}(Z_{Fe/H}, z)$ with high-SFRD and (because of the FMR) low $Z_{\text{Fe/H}}$, while avoiding the extremes of the distribution.

In Fig. 3, we plot the sample of MW GCs with isochronal ages and $Z_{\text{Fe/H}}$ from VandenBerg et al. (2013). For each cluster, we assume its best-fit age corresponds to the lookback time/z of its formation. We also show $Z_{\text{O/H}}$ measurements for 16 MW GCs from Carretta et al. (2009), noting that GC stars can display large internal spreads in this element. We adopt the $Z_{\text{O/H}}$ values from Monty et al. (2025) (shifted to our solar scale), who restrict the analysis to O-normal populations and apply a +0.15 dex correction to place the estimates on a common abundance scale with other MW samples (namely the GALAH survey Buder et al. 2021a), using Amarsi et al. (2019) as a baseline for their detailed treatment of NLTE effects.

Fig. 3 shows that most of the MW GCs ($Z_{\text{Fe/H}}$: brown dots; $Z_{\text{O/H}}$: black dots) fall within the corresponding $f_{\text{SFR}}(Z_{\text{Fe/H}},z)$ and $f_{\text{SFR}}(Z_{\text{O/H}},z)$ contours, which enclose the regions where the bulk of stellar mass formed. As expected, none of the GCs are found in the extreme tail of the distribution (dark blue area). However, a few GCs ⁴ fall in the region where, according to our model, star formation occurs almost exclusively in galaxies with $M_* < 10^8 \, M_\odot$. This is somewhat surprising, as such low-mass systems are generally not thought capable of (efficiently or at all) forming the massive (initially $\gtrsim 10^6 \, M_\odot$) star clusters that are the progenitors of present-day GCs (Renaud 2018; Krumholz et al. 2019; Adamo et al. 2020b). Interestingly, *all* of the GCs which fall in this region have been tagged as accreted clusters based on

⁴ NGC4590, NGC5053, NGC5466, NGC6341, NGC7078, NGC7099, and Terzan 8

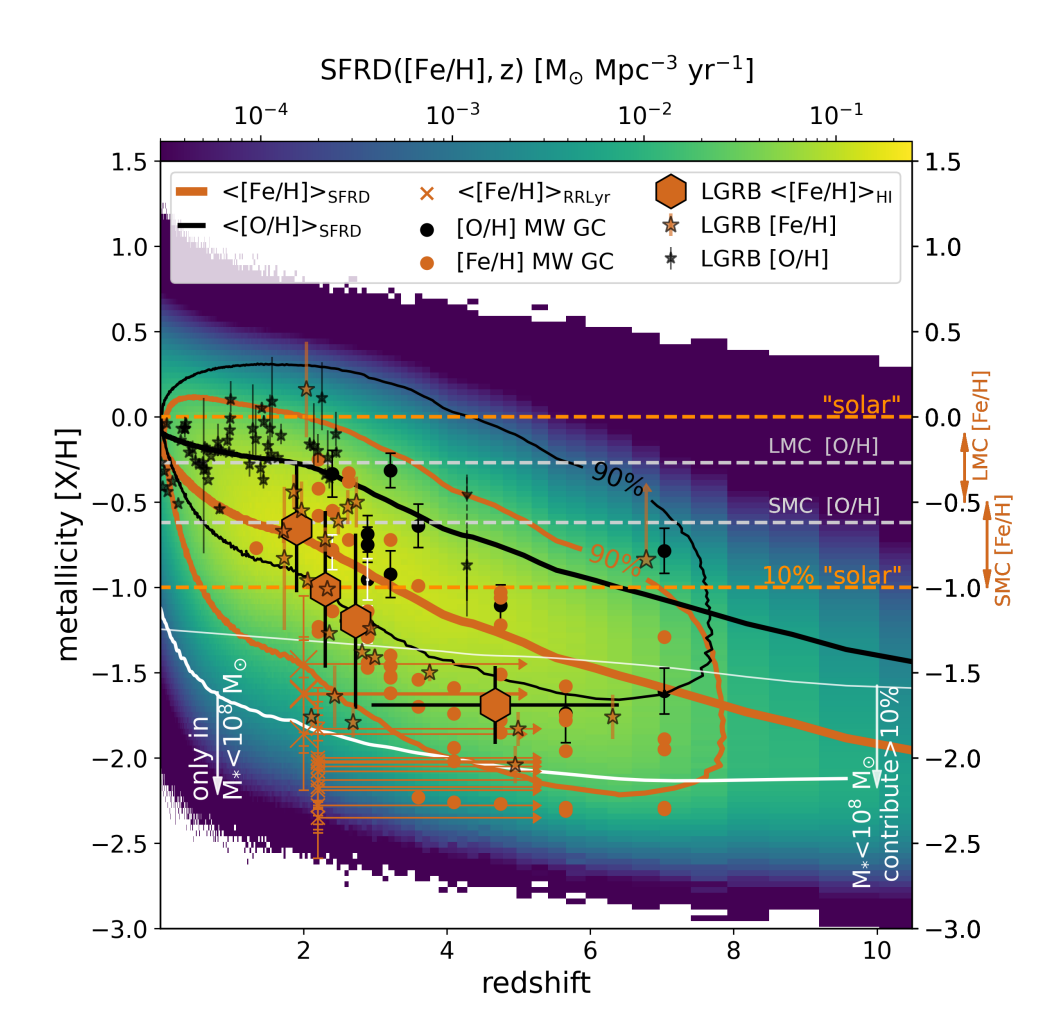


Fig. 3. Distribution of the cosmic SFRD at different [Fe/H] and z (color scale), shown for an example variation described in Sec. 2 Black/brown lines: SFRD-weighted average [O/H] / [Fe/H] at each z. Black/brown contours enclose 90% of the SFRD to further show the offset between the $f_{\rm SFR}([O/H],z)$ and $f_{\rm SFR}([Fe/H],z)$. White solid lines: [Fe/H] below which $M_* < 10^8 M_{\odot}$ galaxies contribute at least 10% of the SFRD (thin line) and below which contribution of $M_* > 10^8 M_{\odot}$ galaxies is negligible (thick line). Data points: cross-check samples introduced in Sec. 3.1. Hexagons: $\langle [Fe/H]\rangle_{\rm HI}$ of LGRB hosts binned in z. Brown/black stars: [Fe/H]/[O/H] of individual LGRB hosts. Crosses: mean [Fe/H] of RR Lyrae stars in local dwarf galaxies (small/big: $M_* < 10^8 M_{\odot}$ / $M_* \gtrsim 10^8 M_{\odot}$, offset for visibility) but formed at z > 2-5 (horizontal arrows). Brown/black dots: [O/H]/[Fe/H] of MW globular clusters. [O/H] and [Fe/H] of the LMC and SMC on our solar scale are indicated for the reference.

their orbits, the chemistry of their O-normal population, or using a combination of both orbits and chemistry (Massari et al. 2019; Massari 2025; Belokurov & Kravtsov 2024; Monty et al. 2024). A more detailed discussion is beyond the scope of this paper, but we return to this comparison in our follow-up study.

3.1.3. Long gamma ray burst hosts: (lower limit on the) $\langle {\rm [Fe/H]} \rangle_{\rm SFRD}(z)$

Long-duration GRBs are typically linked to the deaths of massive stars and are found in actively star-forming regions (e.g. Galama et al. 1998; Hjorth et al. 2003; Christensen et al. 2004; Fruchter et al. 2006). They are among the most energetic electromagnetic transients known and have been detected out to $z \gtrsim 8$ (Tanvir et al. 2009), probing star-forming environments across cosmic time. LGRB afterglows allow determination of the gasphase $Z_{\rm Fe/H}$ in their hosts via absorption-line spectroscopy (e.g. Vreeswijk et al. 2004). This is especially valuable for our study, since direct constraints on $Z_{\rm Fe/H}$ in high-z star-forming environments are scarce. Furthermore, unlike galaxies selected in conventional surveys, LGRB-afterglow selected systems are not ex-

pected to be biased against faint objects.

We use absorption-derived LGRB host properties (total metallicity - $[M/H]_{tot}$, z, and HI column density - N_{HI}) compiled by Heintz et al. (2023), covering 1.7 < z < 6.3. We also include GRB 050505 at $z \approx 4.28$ (Berger et al. 2006, as reanalyzed by Inkenhaag et al. 2025), and GRB 240218A at $z \approx 6.78$, for which, however, only the lower limit of $[M/H]_{tot} \ge -0.8$ is available (Saccardi et al. 2025, revised analysis). Importantly, $[M/H]_{tot}$ represents the total metallicity (gas + dust) of the ISM, corrected for dust depletion (e.g. De Cia et al. 2016, 2018). This correction is critical for iron, which is strongly depleted into dust grains (by 90-99% in the MW e.g. Jenkins 2009, and up to 90% in lower-metallicity environments, e.g. De Cia et al. 2016; Konstantopoulou et al. 2024). $[M/H]_{tot}$ is equivalent to a dustcorrected [Fe/H] when Zn abundance is available to guide the dust correction. If this is not the case, S or Si can be used for dust corrections, but such estimates are more approximate and the resulting $[M/H]_{tot}$ may overestimate $Z_{Fe/H}$ unless α -enhancement is explicitly accounted for (Saccardi et al. 2023; De Cia et al. 2024). We assume that the $[M/H]_{tot}$ values obtained with Znbased dust corrections (i.e. GRB 240218A, and 21 of the 36 obWe also assume that this is the case for GRB 210905A, as its $[M/H]_{\text{tot}}$ accounts for α -enhancement (Saccardi et al. 2023). We plot the [Fe/H] estimates for individual LGRB hosts in this sample in Fig. 3 and we use those estimates (without the lower limit from GRB 240218A) to re-derive the N_{HI} -weighted mean $\langle \text{[Fe/H]} \rangle_{\text{HI}}$ with z, following Eq. 2 of Heintz et al. (2023) (see Tab. E.1 in the appendix for the binning and values). In Sec. 6 we also show $\langle \text{[M/H]} \rangle_{\text{HI}}$ obtained for the full sample. Weighting by N_{HI} accounts for the varying amounts of potentially star-forming gas in the probed galaxies. This enables a comparison between $\langle \text{[Fe/H]} \rangle_{\text{HI}}(z)$ and the $\langle \text{[Fe/H]} \rangle_{\text{SFRD}}(z)$ derived from our models. However, the comparison is complicated by the fact LGRB progenitors are theorized to be massive, iron-poor stars (Hirschi

jects from Heintz et al. 2023) provide a reliable proxy for Z_{Fe/H}.

et al. 2005; Yoon & Langer 2005; Woosley & Heger 2006, but see Chrimes et al. 2020; Briel et al. 2025). Thus, they may preferentially occur in regions of high star formation and low $Z_{\text{Fe/H}}$. Empirical studies indicate a decline in LGRB occurrence near solar metallicity, but overall find no clear cutoff or preference for extremely metal-poor environments (e.g. Vergani et al. 2015; Japelj et al. 2016; Perley et al. 2016; Graham et al. 2023; Disberg et al. 2025) and at intermediate redshifts, LGRB host galaxies appear to trace the star-forming population (Krogager et al. 2024, selected by having cold gas and active starformation). In the presence of such biases, the LGRB-based $\langle \text{[Fe/H]} \rangle_{\text{HI}}$ pro-

vides a lower limit on the overall $\langle [Fe/H] \rangle_{SFRD}$ and we expect the

offset between the two to decrease toward high z, where galaxies

have higher SFRs and lower $Z_{\rm Fe/H}$. Finally, while we focus on $Z_{\rm Fe/H}$, in Fig. 3 we also show $z \lesssim 2.5$ LGRB hosts with emission-line $Z_{\rm O/H}$ estimates from Graham et al. (2023) (obtained with Curti et al. 2017, 2020 calibration, shifted by +0.2 dex for consistency with our scale) and GRB 050505 (Inkenhaag et al. 2025), for which we show the range of $Z_{\rm O/H}$ obtained with different methods. We note that samples with emission-line based $Z_{\rm O/H}$ are subject to the usual selection effects, favoring brighter (more massive, lower redshift) sources. We refer the interested reader to Disberg et al. (2025) for a recent detailed discussion of the comparison with this sample.

Based on the comparison shown in Fig. 3 we note the following:

- Z_{Fe/H} and Z_{O/H} of individual LGRB hosts show appreciable scatter, which our model fully accounts for.
- $\langle [Fe/H] \rangle_{HI}$ from absorption-derived LGRB host properties does not trace $\langle [O/H] \rangle_{SFRD}$. However, $\langle [Fe/H] \rangle_{SFRD}$ is broadly consistent with $\langle [Fe/H] \rangle_{HI}$.

The second point demonstrates the importance of accounting for non-solar abundance ratios when comparing "metallicities" probed by different elements, particularly in the context of the potential low metallicity bias of LGRB. Our model predicts a milder evolution than the LGRB-based estimate in the highest-z bin; however, $\langle [Fe/H] \rangle_{HI}$ estimate in this bin is likely unreliable (see Sec. 6, where we also compare across model variations), and we refrain from drawing conclusions from comparison in this z range.

4. How (un)common is the solar abundance pattern?

The example discussed in Sec. 3 shows a persistent offset between $\langle [O/H] \rangle_{SFRD}$ and $\langle [Fe/H] \rangle_{SFRD}$, i.e. the SFRD-weighted mean $\langle [O/Fe] \rangle_{SFRD} > 0$ at all redshifts. This indicates that most of the cosmic star formation happened with O/Fe ratio larger than 'solar'. We quantify this result and its sensitivity to assumptions about the uncertain factors in our model in Fig. 4.

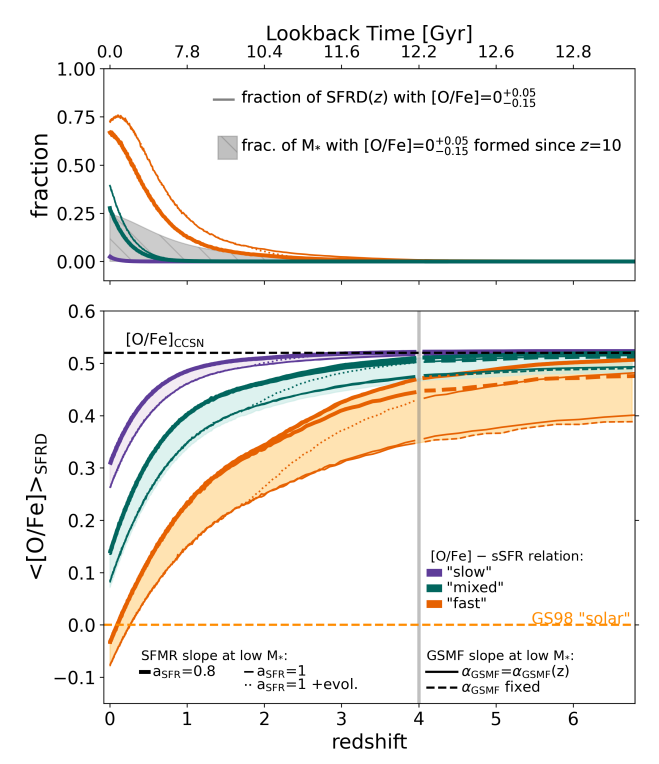


Fig. 4. Top: The gray area indicates that, across our models, the fraction of cosmic stellar mass formed since z=10 with near-solar [O/Fe] (between –0.15 and 0.05 dex) is at most 30%. Lines show the fraction of the total SFRD(z) formed with near-solar [O/Fe]. Bottom: SFRD weighted mean [O/Fe] as a function of redshift/lookback time. At z < 4 (z > 4), the line styles distinguish between the assumptions about the SFMR (α_{GSMF}). Colors indicate the [O/Fe]–sSFR relation and the colored areas indicate the range spanned by models with a fixed [O/Fe]–sSFR relation. Green dotted line corresponds to our example variation.

The [O/Fe]-sSFR relation represents the dominant source of uncertainty in the $\langle [O/Fe] \rangle_{SFRD}$ and in the fraction of the SFRD with 'near-solar' O/Fe abundance ratios, liberally defined here as a range between [O/Fe]=-0.15 and 0.05 dex $(log_{10}(O/Fe)$ =1.18 -1.38) to enclose different reference solar abundance ratios used in the literature ⁵. Colors in Fig. 4 correspond to different average [O/Fe]-sSFR relations, varied between the extreme cases discussed in Sec. 2.1. The $\langle [O/Fe] \rangle_{SFRD}$ approaches the solar value only in the 'fast' Fe-enrichment scenario (orange curves), which assumes the minimum possible delay between CCSN and the onset of enhanced Fe enrichment. Even in this case, $\langle [O/Fe] \rangle_{SFRD} \lesssim 0$ only at $z \lesssim 0.4$. On the other extreme, using the [O/Fe]-sSFR relation corresponding to the 'slow' Fe-enrichment scenario (purple curves) leads to $\langle [O/Fe] \rangle_{SFRD} \gtrsim 0.25$ dex even at z=0 and the fraction of SFRD(z=0) with 'near-solar' O/Fe ratio is $\lesssim 2\%$. We note that the fraction of cosmic stellar mass formed with near-solar [O/Fe] is the most sensitive to the [O/Fe]-sSFR relation around $log_{10}(sSFR) \sim -9$ (i.e., main-sequence galaxies at $z \sim 0.6$ –2). Only a steeper drop to solar-like [O/Fe] in this regime can visibly increase this fraction. However, a relation steeper in this regime than our extreme "fast" Fe-enrichment scenario would challenge the current constraints on the relation (see Fig. 1 and Ch24). Variations in the shape of the relation at lower sSFR have only a marginal impact, because such galaxies contribute little to the (integrated) cosmic SFRD budget.

 $^{^5}$ $Z_{\rm Fe/H}$ = 7.45 - 7.5 and $Z_{\rm O/H}$ = 8.69 - 8.83 (Lodders et al. 2009; Asplund et al. 2009, 2021; Grevesse & Sauval 1998), leading to -0.15 to +0.05 offsets in [O/Fe] relative to our scale.

Another factor important for those results is the distribution of galaxy sSFR: a higher fraction of galaxies with high sSFR increases $\langle [O/Fe] \rangle_{SFRD}$, whereas weaker evolution in galaxy sSFR with z leads to weaker evolution of $\langle [O/Fe] \rangle_{SFRD}$. To quantify this effect, in Fig. 4 we consider three variations of the SFMR (shown in Fig. 6): the relation from P23 (thin solid lines), the same relation but with a shallower slope a_{SFR} =0.8 instead of $a_{\rm SFR}$ =1 at low M_* (thick solid lines), and a version with increased high-z evolution (dotted lines; as in the example in Sec. 3). We vary $a_{\rm SFR}$ because (i) our analysis extends to galaxies with M_{*} much lower than $\log_{10}(M_*/M_{\odot})>8.7$ adopted in P23 to restrict their fit to regimes with high sample completeness, and (ii) a_{SFR} has a strong impact on our results: adopting a_{SFR} =0.8 instead of $a_{SFR}=1$ leads to ~ 1 dex higher $\log_{10}(SFR)$ at $M_*=10^6 M_{\odot}$. While observational studies report even lower a_{SFR} values (particularly at high z, see e.g. compilations in Speagle et al. 2014; Boogaard et al. 2018; Mérida et al. 2023), Simmonds et al. (2025) attribute these to sample incompleteness, while Leja et al. (2015) argue that such shallow slopes are inconsistent with the observed evolution of the GSMF (see also Di Cesare et al. 2025). Moreover, assuming $a_{SFR} < 0.8$ would cause a significant overestimate of the cSFH (see Sec. 5.1). The effect of a_{SFR} and/or galaxy sSFR evolution on $\langle [O/Fe] \rangle_{SFRD}$ can be partially offset by the abundance of low- M_* galaxies. In our framework, the latter is tied to uncertain low- M_* slope of the GSMF. Assuming fixed α_{GSMF} (lines continued as dashed at z > 4) versus $\alpha_{\text{GSMF}}(z)$ that steepens with z has a relatively small effect on the results shown in Fig. 4. Finally, we point out that:

- The fraction of mass formed in stars until the present day with [O/Fe] between -0.15 dex and 0.05 dex is at most 25% (gray band, top panel in Fig. 4).
- The fraction of cosmic SFRD happening with 'near-solar' [O/Fe] is negligible at z > 2 across our models. This fraction is negligible even at $z \sim 0$ if the delay between the CCSN enrichment and enhanced Fe production is long (O(10^8 yr)).

The exact values shown in the top panel of Fig. 4 depend to some degree on how we model the metallicity scatter within galaxies (see Appendix D). We show that even under the extreme assumption that the stellar $Z_{\text{Fe/H}}$ and $Z_{\text{O/H}}$ distributions within a host are fully independent (which considerably broadens the SFRD distribution in [O/Fe] at each z), the fraction of mass formed with near-solar [O/Fe] remains < 30%. Thus, the specific treatment of scatter does not affect our main conclusion that star formation with near-solar [O/Fe] is rare. This is in stark contrast to the fact that most stellar evolution and spectral synthesis models used in the literature, and applied to interpret observations, including those of young and high-z environments, assume a solar abundance pattern (in particular, $[\text{O/H}] \approx [\text{Fe/H}] \approx \log_{10}(Z/Z_{\odot})$). We discuss the implications of this result in Sec. 7.

4.1. The relevance of the solar abundance pattern

Figure 5 shows that the results discussed above are consistent with the MW being representative of the star-forming population, and the Sun's abundances being common for stars formed in such galaxies 4-5 Gyr ago.

In our model, MW-like mass galaxies are among the dominant contributors to the cosmic SFRD at $z \lesssim 2$, consistent with the view that the MW and its progenitors are L*-like systems. Using the FMR (Fig. 2) at a lookback time of 4–5 Gyr, the gas-phase $Z_{\rm O/H}$ for MW-like galaxies is [O/H]=0.1 dex, which would make the Sun appear mildly 'O-poor' relative to typical stars formed at that epoch (adopting a different $Z_{\rm O/H\odot}$ than our reference value

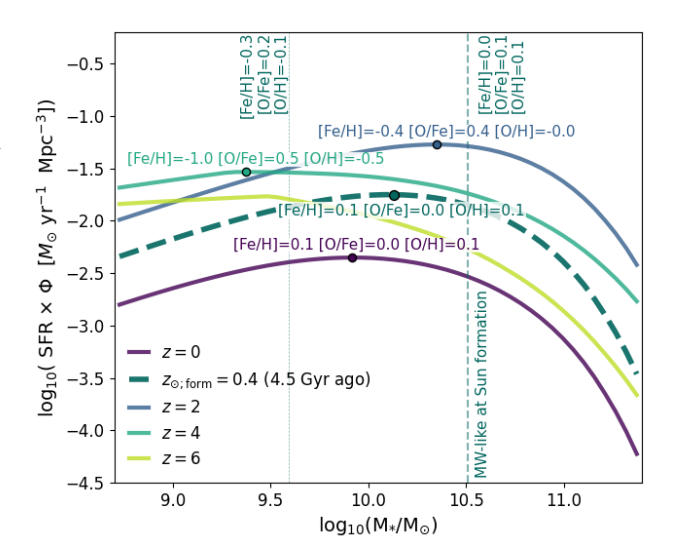


Fig. 5. Contribution to the cosmic SFRD (SFR density per $\log M_*$ bin) versus galaxy $\log_{10}(M_*)$ at several z (colors; bottom and top curves correspond to z=0 and z=2, respectively, reflecting the cSFH evolution). Filled circles mark the $\log_{10}(M_*)$ at which the contribution peaks at each z (ill-defined for z >4). At each marked mass we list the typical abundances ([O/Fe],[O/H],[Fe/H]) of star-forming gas in our model. The thick dashed curve highlights $z \approx 0.4$, corresponding to a lookback time of 4.5 Gyr (the epoch of Solar birth). Vertical dashed lines show $\log_{10}(M_*)$ within ± 0.1 dex of the z = 0.4 peak; abundances for these two masses are reported at the top. This brackets MW-mass galaxies that, at Solar birth, were forming stars with close to solar abundance ratios. Shown for our example variation.

from Grevesse & Sauval (1998) would generally make this off-set larger). Given the Sun's Galactocentric distance of $\gtrsim 1.5R_e$ and the negative $Z_{\rm O/H}$ gradients commonly observed in spirals, the Sun may have formed at a lower $Z_{\rm O/H}$ than the global value inferred from galaxy scaling relations. Ch24 estimate a possible ~ -0.05 dex offset due to the MW gradient from (Arellano-Córdova et al. 2020), similar to the abundance spread found for solar-like (in terms of age and [Fe/H]) disk stars (Nissen 2015). Moreover, a 0.1 dex offset in $Z_{O/H}$ is also comparable to the intrinsic scatter of the $Z_{O/H}$ -MZR ($\sigma_{\rm MZR} \approx 0.1$ dex at high M_*), meaning that MW-like galaxies with [O/H]=0 lie within the typical population at $z \lesssim 0.4$.

The abundance values in Fig. 5 are reported for our example variation, in particular, assuming the "mixed" Fe enrichment scenario. The [O/Fe]-sSFR relation dominates the uncertainty of those results: adopting an alternative relation leaves [O/H] unchanged but shifts both [Fe/H] and [O/Fe] for the MW-like galaxy at z = 0.4 by ± 0.2 dex, making the Sun appear 'Fe-poor' (fast Fe enrichment) or 'Fe-rich' (slow Fe enrichment) relative to the typical abundances we assign at its birth epoch. Such shifts are comparable to the dispersion of the solar-neighborhood thindisk Z_{Fe/H}-metallicity distribution function (MDF) at fixed age (~0.15 - 0.2 dex Casagrande et al. 2011; Hayden et al. 2015; Buder et al. 2021b; Feuillet et al. 2019). The intrinsic scatter in $Z_{Fe/H}$ -MZR for MW-mass galaxies and the MW $Z_{Fe/H}$ gradient are comparable to those for $Z_{O/H}$ (e.g. Gallazzi et al. 2005; Spina et al. 2021), similar offsets in $Z_{Fe/H}$ are therefore expected within the population. In principle, all our model variations predict the formation of stars with solar abundance ratios in MWlike galaxies at the solar formation epoch, within the expected scatter. However, such stars need not align with the MDF peak in MW-like galaxies. The match is closest for [O/Fe]-sSFR relation intermediate between our "mixed" and "fast" Fe-enrichment scenarios, and poorest if the relation resembles the "slow" Feenrichment case. In the latter case, negative radial metallicity gradients would further exacerbate deviations from solar $Z_{\text{Fe/H}}$ and $Z_{\rm O/H}$. Zooming out to cosmic volume, depending on the [O/Fe]-sSFR relation, stars with [O/Fe]=0 at the solar formation epoch would either coincide with the peak of the [O/Fe] distribution ("fast", Fig. G.3), lie within the region enclosing 95% of the cosmic SFRD ("mixed", Fig. G.2), or fall outside the contours enclosing 99% of the cosmic SFRD ("slow"). A detailed comparison of our work with the MW requires careful accounting for selection effects, completeness, and systematics in MW stellar surveys, and is beyond the scope of this paper. For the purposes of this discussion, we note that if the MW is representative of star-forming galaxies, and if the near-solar $Z_{O/H}$ and $Z_{Fe/H}$ values are typical of stars formed in such systems at $z \leq 0.4$, then our 'slow' Fe-enrichment scenario is disfavoured.

5. Cosmic star formation history: model variations

5.1. Total cosmic star formation history

In the right panel of Fig. 6, we show the cSFH obtained under different combinations of assumptions in our model together with literature observational estimates. This serves as an important consistency check: although our framework is based on empirical relations, it does not include any normalization to match independent constraints on the cSFH when these relations are combined. The observational data shown include UVbased estimates (blue data points) compiled by Madau & Dickinson (2014), and the recent z > 6 estimates from Rinaldi et al. (2022) (lower limit based on the galaxies in the COS-MOS/SMUVS catalogue), Donnan et al. (2024), Whitler et al. (2025) and Chemerynska et al. (2024) (all three based on integration of the UV luminosity functions to the same limiting magnitide $M_{UV} = -17$). Additionally, we show the IR/(sub)millimeter based estimates (red data points/limits) compiled by Casey et al. (2018), and the estimates from Gruppioni et al. (2020), Loiacono et al. (2021), Khusanova et al. (2021) and Algera et al. (2023). These studies sample the contribution of dusty star-forming galaxies, constraining the obscured fraction of the SFRD to $z \sim 7$. Martis et al. (2025) probe the obscured fraction with photometry up to z = 9, finding that ~50% of all SFR up may still be obscured by at those early epochs, and thereby would be missed by the UV luminosity function-based SFRD estimates.

As in the previous section, we vary the contribution of low- M_* galaxies by changing $\alpha_{\rm GSMF}$ (see top left panel in Fig. 6) and $a_{\rm SFR}$ and we consider increased $z \gtrsim 2$ evolution of the SFMR with respect to P23 (bottom left panel in Fig. 6). In gray we also show the cSFH obtained assuming a high SB contribution (see appendix B), motivated by the results of Caputi et al. (2017); Rinaldi et al. (2022, 2025) who find a SB fraction $f_{SB}(M_*, z)$ that strongly increases with z and to low M_* .

Direct comparison of our results with the literature is complicated by methodological differences, which can readily introduce offsets of order a few in the estimated SFRD. Properly accounting for these differences is beyond the scope of this work. For this reason, we do not exclude any model variations that are consistent with literature SFRD estimates within a factor of 10. SFRD estimates are particularly sensitive to the assumed lower limit of the integration, whether in M_* (our estimates) or in IR/UV luminosity (literature), where galaxy properties are uncertain. To illustrate this, we show in Fig. 6 (hatched regions) the

effect of raising the lower integration limit from $M_{min}=10^6 M_{\odot}$ to $M_{min}=10^8 M_{\odot}$ for several variations. The impact grows with z, as does the apparent mismatch with literature estimates, reaching a factor of 3–5 at z=8 for models with evolving $\alpha_{\rm GSMF}(z)$ and $\alpha_{\rm SFR}=0.8$ or with high SB contribution (both elevate SFR at $M_*<10^9 M_{\odot}$). By contrast, for $\alpha_{\rm GSMF}=\alpha_{\rm fix}$, the effect is negligible to $z \ge 9$.

We note that a high SB contribution would lead to an overestimate of the SFRD at z > 2 by a factor >10 compared to literature values, even for $M_{min} = 10^8 M_{\odot}$, unless $a_{SFR} \gtrsim 1$ (which is not the case in Rinaldi et al. 2022, 2025). Such variations are not considered further. The limiting case with high f_{SB} and $a_{SFR} = 1$ (hereafter 'high f_{SB} ') is, for our results, effectively indistinguishable from a scenario without an SB sequence but with a_{SFR} evolving with z ($a_{SFR} \sim 0.9$ at z = 0 and $a_{SFR} \lesssim 0.8$ at z > 2). The corresponding results are qualitatively similar to those for the $a_{SFR} = 0.8$ case and, for clarity, we do not show them in all figures. Finally, while our analysis does not extend beyond z > 10.5, in Fig. 6 we show the cSFH up to $z \sim 13$ to highlight its strong dependence on the extrapolation of the GSMF (see Appendix A).

5.2. "Low-metallicity" cosmic star formation history

The "low-metallicity" cSFH (obtained by considering cosmic SFRD only below some metallicity threshold) is where the differences between oxygen- and iron-based results are most pronounced. The dotted lines in the right panel of Fig. 7 illustrate this for the example variation discussed in Sec. 3, and compare the total (top line) and the "low-metallicity" cSFH traced by either $Z_{\text{Fe/H}}$ (middle line) or $Z_{\text{O/H}}$ (bottom line). These are obtained by integrating $f_{SFR}(Z_{Fe/H}, z)$ and $f_{SFR}(Z_{O/H}, z)$ (shown in Figs. 3 and G.1) up to the same relative "low-metallicity" threshold, [Fe/H] = [O/H] = -0.65, defined as the logarithm of the elemental abundance relative to solar. This threshold is chosen arbitrarily, but roughly selects sub-SMC metallicity environments⁶. For the example variation, nearly all SFRD at $z \gtrsim 4$ happens below the SMC-like [Fe/H], whereas this occurs at $z \gtrsim 8$ if this threshold is defined in terms of oxygen abundance. The orange and blue regions shown in Fig. 7 span the cosmic SFRD below [Fe/H] < -0.65 and [O/H] < -0.65, respectively, calculated across model variations and illustrating the associated uncertainties. While the quantitative outcome depends on the chosen metallicity threshold (with lower thresholds yielding larger uncertainties) the qualitative behavior remains consistent with that described for the example variation. The overlap between the two ranges increases with z as the fraction of SFRD below the metallicity threshold approaches the total (gray area), occurring at lower z for iron- than for oxygen-based cut. When compared for the same relative threshold, the SFRD is higher at "low" $Z_{Fe/H}$ than at "low" $Z_{O/H}$, and the low- $Z_{Fe/H}$ cSFH peaks at lower z than its oxygen counterpart.

At $z \le 4$, the orange range is wider than the blue one due to additional uncertainty introduced by the [O/Fe] – sSFR relation. As shown in Sec. 4, in the "fast"/"slow" Fe-enrichment scenario (orange/purple lines in the left panel in Fig. 7), the difference between the $f_{\rm SFR}(Z_{Fe/H},z)$ and the $f_{\rm SFR}(Z_{O/H},z)$ (therefore, also between low- $Z_{\rm Fe/H}$ and low- $Z_{\rm O/H}$ cSFH) is the smallest/largest. Other assumptions, highlighted in the right panel in Fig. 7, affect both $f_{\rm SFR}(Z_{Fe/H},z)$ and $f_{\rm SFR}(Z_{O/H},z)$. The assumed

⁶ Here we assume the SMC gas phase $Z_{\rm O/H}$ ≈8.2 and $Z_{\rm Fe/H}$ =6.85 ([Fe/H]=-0.65 on our solar scale) as in Ch24. However, a broad range of [Fe/H]≈-1 to -0.5 were reported for young SMC stellar samples with ages of a few Myr (e.g. Romaniello et al. 2008; Narloch et al. 2021).

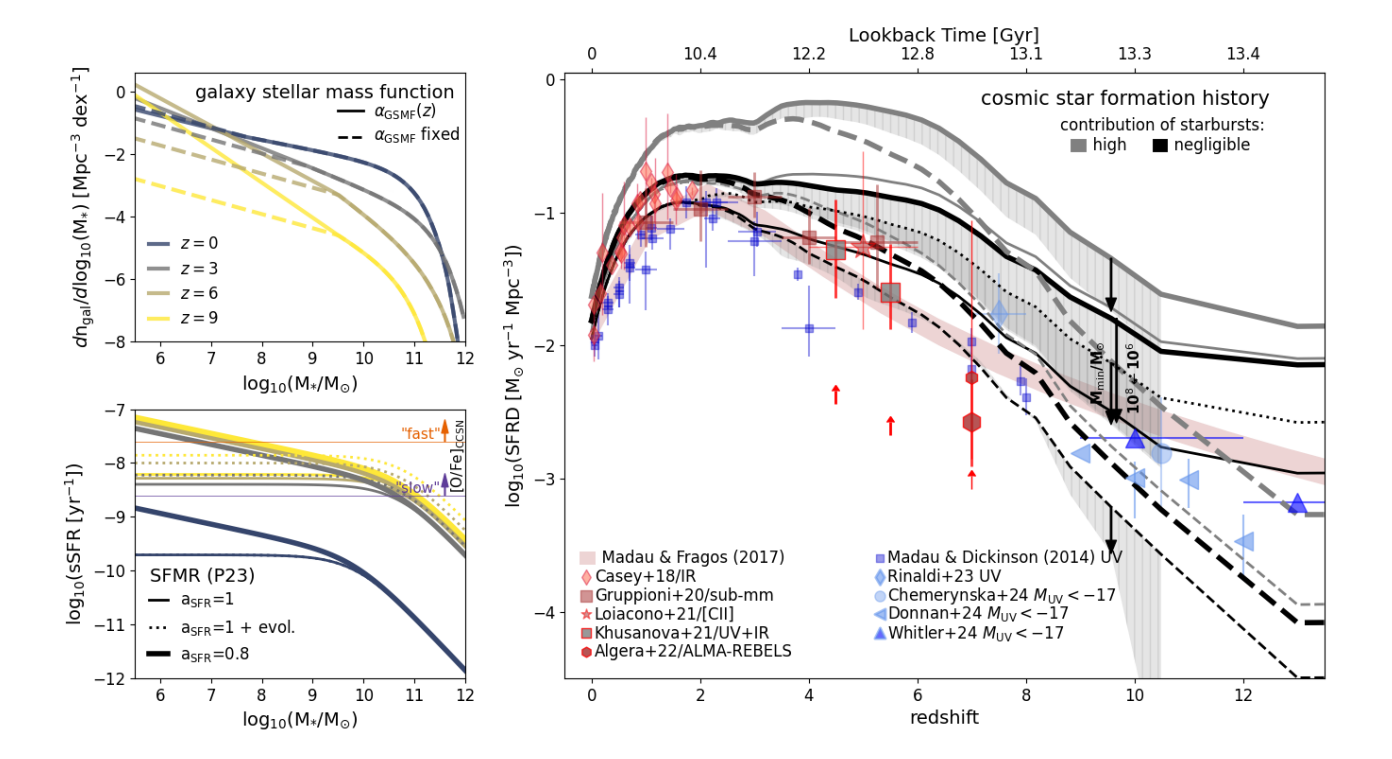


Fig. 6. Right: cSFH for different combinations of assumptions about the GSMF (solid/dashed lines: $\alpha_{\rm GSMF}$ steepening with z/ fixed), SFMR (thin/thick lines: P23 with $a_{\rm SFR}$ =1/ $a_{\rm SFR}$ =0.8, dotted line: P23 with additional evolution at z>2) and the contribution of SB (black/gray lines -negligible/high). Data points - observational estimates (see legend), red band - estimate from Madau & Fragos (2017). Where necessary, we adjust the literature estimates to Kroupa (2001) IMF assumed here. Hatched regions illustrate the effect of increasing the lower limit of integration from $10^6 M_{\odot}$ to $10^8 M_{\odot}$. Dotted line shows the cSFH of the variation considered in Sec. 3. Top left: GSMF variations for different z (colors). Bottom left: SFMR variations in the log₁₀(sSFR) - log₁₀(M_{*}) plane for different z (colors, as in top

Top left: GSMF variations for different z (colors). Bottom left: SFMR variations in the $log_{10}(sSFR) - log_{10}(M_*)$ plane for different z (colors, as in top left). Thin horizontal lines mark $log_{10}(sSFR)$ above which galaxies following the corresponding [O/Fe]-sSFR relation reach [O/Fe]=[O/Fe]_{CCSN}.

non/evolution of the FMR at z>4 has a negligible effect on those results compared to $\alpha_{\rm GSMF}$ and $a_{\rm SFR}$.

An alternative approach to comparing $f_{SFR}(Z_{Fe/H}, z)$ and $f_{SFR}(Z_{O/H}, z)$ (which avoids the need for a metallicity threshold) is to examine their metallicity distribution functions (MDFs), obtained by integrating the distributions over selected redshift ranges. This view can help inform the initial metallicity distribution assumptions in models of stellar or prompt-transient populations formed within specific time ranges and serve as a reference for comparison with observed or simulated galactic MDFs. We discuss the MDFs for our models for selected redshift intervals in Appendix F.

6. <[Fe/H]>: models and constraints from LGRBs

In Fig. 8, we show $\langle [Fe/H] \rangle_{HI}$ derived from absorption-based LGRB host properties against $\langle [Fe/H] \rangle_{SFRD}$ from our model variations. As discussed in Sec. 3.1.3, LGRB host sample is not selected by galaxy brightness (i.e. is not expected to be biased against faint galaxies) and additionally, LGRBs may preferentially occur in low-[Fe/H] and/or high-SFR environments. Consequently, $\langle [Fe/H] \rangle_{HI}$ could be biased to lower values relative to $\langle [Fe/H] \rangle_{SFRD}$ but the offset should *decrease* with *z* as LGRB-selected galaxies become increasingly representative of the general star-forming population. In this view, models predicting $\langle [Fe/H] \rangle_{SFRD}$ that fall below or diverge from the LGRB-based average at high *z* are disfavored. The current limited sample size and the significant scatter within each *z* bin (as indicated by the errors in $\langle [Fe/H] \rangle_{HI}$, representing the standard deviation)

prevent us from drawing firm conclusions about any of the model variations. Nonetheless, we note the following:

- Assuming a 0.2 dex lower $Z_{O/H;MZR0}$ (long-dashed gray line; within systematics in the low z gas-phase $Z_{O/H}$ calibrations), would cause variations assuming "slow" Fe enrichment (bottom panel) to fall below the LGRB-based average in the lowest z bin, which is not expected.
- At $z \le 3$, our estimates of $\langle [Fe/H] \rangle_{SFRD}$ are the most sensitive to the adopted [O/Fe]-sSFR relation. The steeper decline between z=2 and 3 obtained under the "fast" Feenrichment assumption (top panel) appears more consistent with the LGRB-based trend when taken at face value.
- − The underlying LGRB host population appears insufficiently sampled to allow for a reliable estimate of $\langle [Fe/H] \rangle_{HI}$ in the highest-z bin (z=3–6.4). In this bin, the sub-sample of LGRB hosts selected to ensure $[M/H]_{tot} \approx [Fe/H]$ exhibits a much smaller scatter in $[M/H]_{tot}$ compared to both other redshift bins and the full LGRB sample within the same bin. The lower limit on [Fe/H] from GRB 240218A at $z \sim 6.8$ lies ≈ 0.8 dex above the estimated $\langle [Fe/H] \rangle_{HI}$ for z=3–6.4, further indicating that the small observed scatter is not physical and that the inferred $\langle [Fe/H] \rangle_{HI}$ may be biased.

In light of the above, we avoid drawing conclusions from the highest-z bin. However, differences between our model variations become more pronounced in this regime, and future LGRB constraints would offer a valuable test for our framework. We also show the range of $\langle [O/H] \rangle_{SFRD}$ spanned by our models (pale blue region in Fig. 8), which is systematically higher than both $\langle [Fe/H] \rangle_{SFRD}$ and $\langle [Fe/H] \rangle_{HI}$.

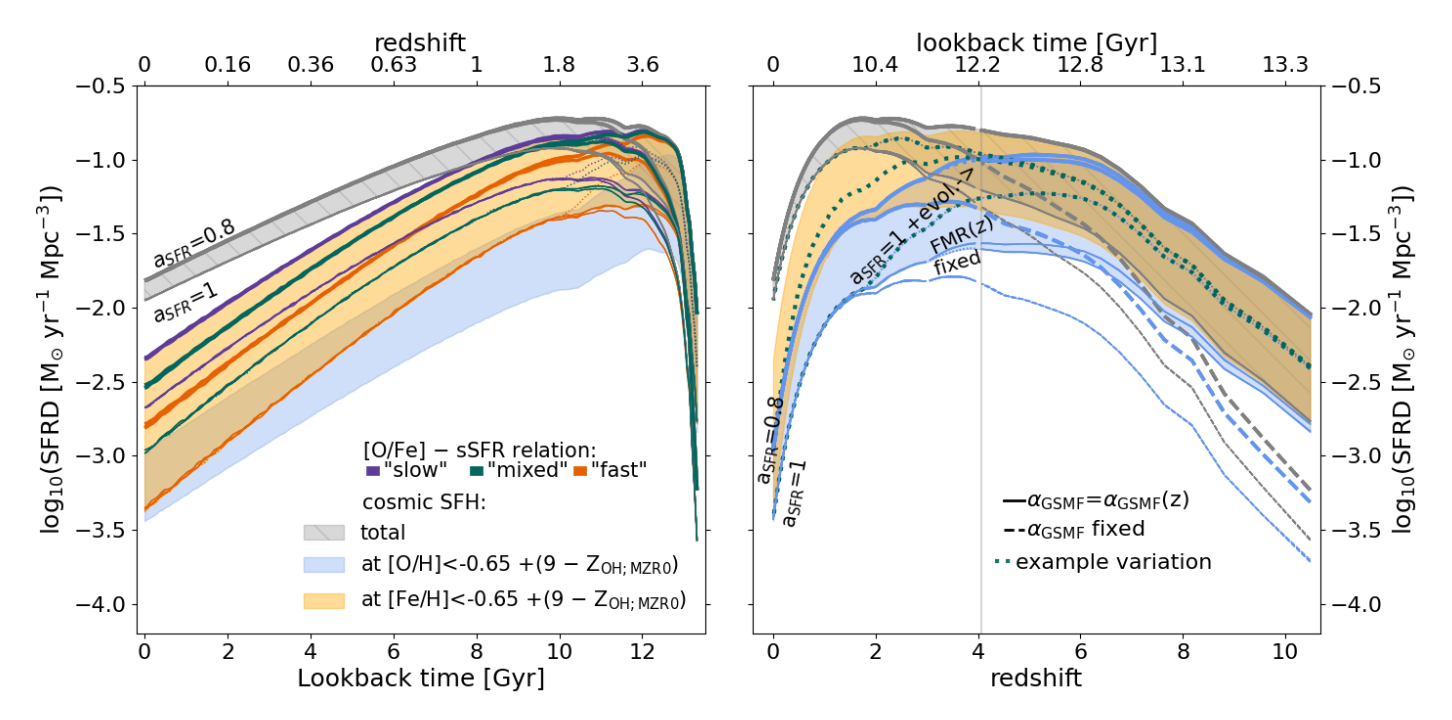


Fig. 7. SFRD as a function of redshift or lookback time. Gray: total; orange/blue: SFRD at [Fe/H]/[O/H] below -0.65 threshold, chosen to roughly select sub-SMC metallicity environments. Shaded regions span the range of results for different model variations with $\alpha_{\rm GSMF}(z)$. The left/right panels use lookback time/z as the primary x-axis to show assumptions most relevant at low/high z. Green dotted lines in the right panel show the cSFH and its [Fe/H]<-0.65 and [O/H]<-0.65 cuts for the example variation discussed in Sec. 3. Other lines highlight selected variations, shown for iron- and oxygen-dependent cSFHs in the left and right panels, respectively. In the right panel, line styles switch to dashed above z = 4 to mark fixed $\alpha_{\rm GSMF}$ variations. Systematics in the $Z_{\rm OH:MZR0}$ translate into shifts of the [O/H] and [Fe/H] thresholds, as shown in the legend.

7. The risks of using solar-scaling

The prevalence of super-solar O/Fe abundance ratios contrasts with the fact that the solar abundance pattern is a common underlying assumption in models of stellar evolution, populations and spectra. That assumption is inherited when such models are used to quantify the effects of stars and stellar populations on their environments and to interpret observations. Enforcing a solar-scaled ratio where it does not apply can introduce systematic errors. The magnitude of these errors is inherently model-dependent, nonetheless, our results can be combined with specific modeling frameworks to quantify the impact in a given application. Here we restrict ourselves to a qualitative discussion and illustrative examples of the expected biases.

7.1. Pedagogical example

In models/simulations, metallicity effects are often parameterized by a simple scaling with the total metal mass fraction relative to solar (Z/Z_{\odot}) . In practice, however, particular elements may dominate "metallicity" effects for different physical processes. In particular, gas cooling is largely determined by the abundance of oxygen (Richings et al. 2014; Katz et al. 2022; Sharda et al. 2023), while the effects of stellar evolution (e.g. feedback, winds) are driven by the abundance of iron (see sec. 7.2). If [O/Fe]=0, one may apply the same scaling to describe both processes, i.e. $n_{O/H}/n_{O/H_{\odot}}$ = $n_{Fe/H}/n_{Fe/H_{\odot}}$ = $Z/Z_{\odot}.$ However, our results show that this is rarely the case. As a simple illustration of the bias introduced by this scaling, one can compare the difference in $n_{O/H}$ and $n_{Fe/H}$ when Z/Z_{\odot} is fixed but computed for an arbitrary [O/Fe] (all the other elements are solarscaled). Assuming [O/Fe]=[O/Fe]_{CCSN}=0.52 and mass fraction of $X_O \approx 0.05$ and $X_{Fe} \approx 0.09$ in the solar composition (Grevesse

& Sauval 1998):

$$\left(\frac{n_{O/H}}{n_{O/H_{\odot}}}\right) / \left(\frac{Z}{Z_{\odot}}\right) = \frac{(X_O + X_{Fe}) \cdot 10^{[O/Fe]}}{X_{Fe} + X_O \cdot 10^{[O/Fe]}} \approx 1.12$$

$$\left(\frac{n_{Fe/H}}{n_{Fe/H_{\odot}}}\right) / \left(\frac{Z}{Z_{\odot}}\right) = \frac{(X_O + X_{Fe})}{X_{Fe} + X_O \cdot 10^{[O/Fe]}} \approx 0.35$$

Thus, using Z/Z_{\odot} scaling would overpredict $n_{O/H}$ -scaled effects by only a small amount (12%) but underpredict $n_{Fe/H}$ -scaled effects by a factor 3 in young and highly star forming environments, biasing modeled cooling and feedback in opposite directions. In general, the difference is larger for elements that contribute less by mass.

7.2. Stellar/multiple evolution

Stellar evolution is sensitive to birth chemical composition predominantly via effect on winds, opacity and nuclear burning efficiency. For stars with $M_{\rm ZAMS} \gtrsim 1.2$, M_{\odot} whose main-sequence burning is CNO-cycle dominated, the nuclear rate depends directly on the total C+N+O abundance (Kippenhahn et al. 2012). The main impact is on the main-sequence lifetime, shortened by a few percent if $Z_{O/H}$ is increased at fixed $Z_{Fe/H}$ (Pietrinferni et al. 2009; VandenBerg et al. 2012). The effects of opacity and linedriven winds are more striking and increasingly important for hot, massive stars. Photospheric and envelope opacities are set largely by Fe-group abundances (Iglesias & Rogers 1996; oxygen dominates only in the cool atmospheres of late-K/M dwarfs and giants) and the radiation-driven winds of hot stars scale with Z_{Fe/H} (e.g. Pauldrach et al. 1993; Kudritzki 2002; Vink & de Koter 2005; Puls et al. 2008; Krtička & Kubát 2018; Vink & Sander 2021; Björklund et al. 2023). Mass loss is weaker at lower $Z_{Fe/H}$, though the scaling also depends on stellar effective temperature, mass and luminosity. Adopting $\dot{M}_{\mathrm{wind}} \propto Z_{Fe/H}^{lpha_{\mathrm{wind}}}$ with $\alpha_{wind} = 0.42/\alpha_{wind} = 0.85$ (Vink & Sander 2021, above/below

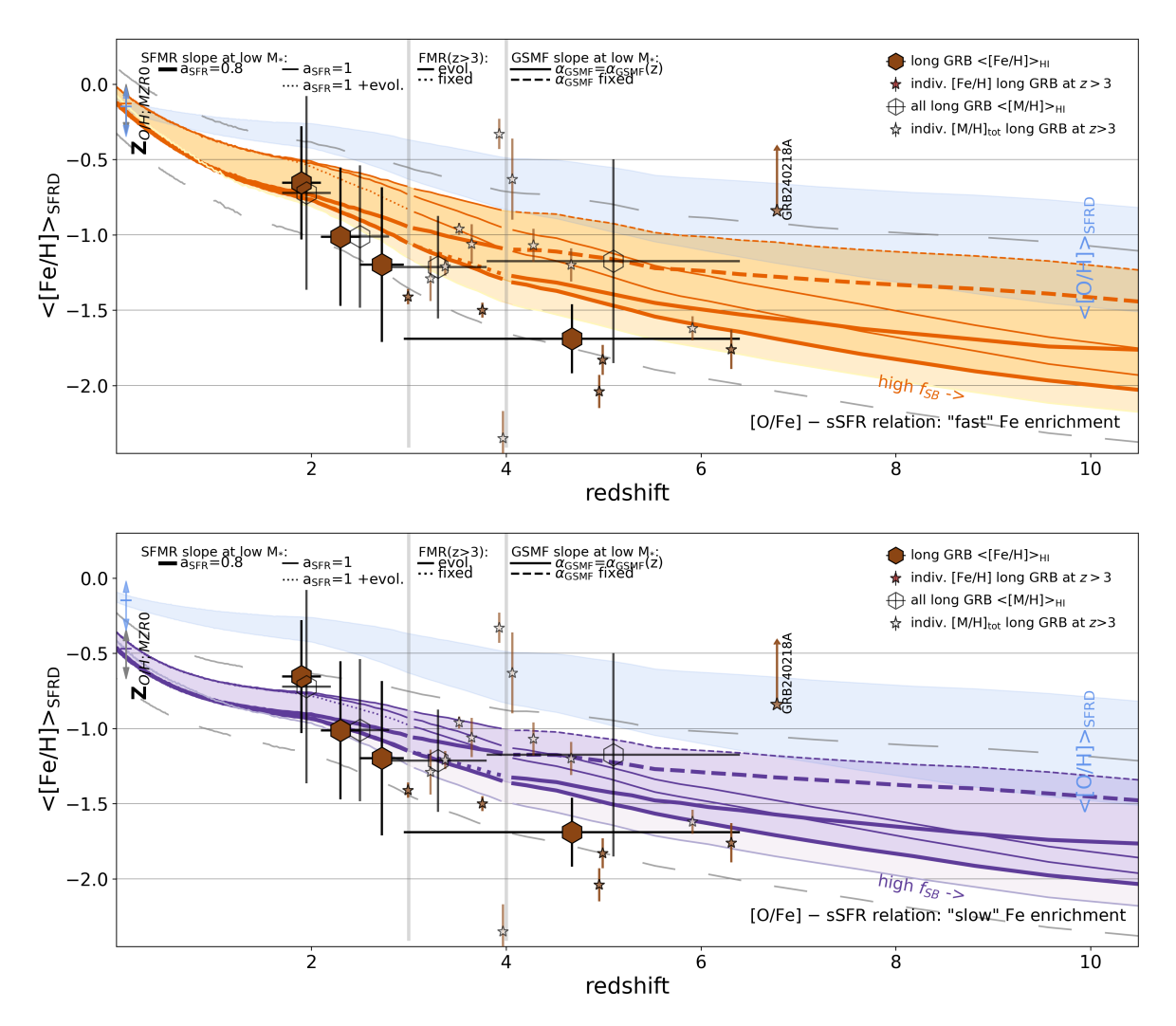


Fig. 8. SFRD-weighted mean $\langle [Fe/H] \rangle_{SFRD}$ as a function of redshift, spanned by our models (orange/purple regions) with selected variations shown as lines. The corresponding $\langle [O/H] \rangle_{SFRD}$ range is shown in pale blue (same in both panels). Top/bottom panels: assuming [O/Fe]–sSFR relation with "fast"/"slow" Fe enrichment. The vertical lines separate three z ranges where the line styles compare different assumptions (see the legend). Data: $\langle [Fe/H] \rangle_{HI}$ from absorption-derived LGRB hosts (filled/open hexagons: subsample with more accurate dust corrections/all, vertical/horizontal errors - standard deviation/z bin width). Stars: individual z > 3 LGRB hosts (brown: with more accurate dust corrections for which $[M/H]_{tot} \approx [Fe/H]$, white: remaining objects, for which $[M/H]_{tot}$ may overestimate [Fe/H]). Vertical arrows - systematics in our estimates due to $Z_{O/H}$ calibration (affecting both $\langle [Fe/H] \rangle_{SFRD}$ and $\langle [O/H] \rangle_{SFRD}$); dashed gray lines show its effect on the edges of the $\langle [Fe/H] \rangle_{SFRD}$ range.

their bi-stability jump), in young and strongly star-forming environments where [O/Fe] \approx [O/Fe]_{CCSN}, one may overestimate \dot{M}_{wind} by a factor of $\sim 1.7-2.7$ using $Z_{O/H}$ as a solar-scaled proxy for Z_{Fe/H}. A more striking yet uncertain example is that of very massive stars (VMS; $\gtrsim 100 M_{\odot}$), which can drive optically thick winds with $\dot{M}_{\rm wind}$ that exceeds that of canonical OB stars (Gräfener & Hamann 2008; Vink et al. 2011; Goswami et al. 2022; Sabhahit et al. 2023; Costa et al. 2025; Martins et al. 2025). Such winds cause a VMS to lose most of its mass over the main sequence. However, constraints are currently lacking at sub-LMC metallicity. Sabhahit et al. (2023) proposed a Z_{Fe/H}-dependent condition for launching strong optically thick winds, which requires the VMS to be more extreme (i.e. more massive and luminous) at lower Z_{Fe/H}. In the presence of such a threshold, incorrectly assigning a metallicity (and thus the wind mode) could affect the masses of the star and the remnant black hole (BH) by an order of magnitude. Using Z_{O/H} as a solar-scaled proxy for Z_{Fe/H} would lead to an overestimation of the strong wind phenomenon in VMS and underestimation of remnant masses - particularly at low $Z_{Fe/H}$. In summary,

 $Z_{\rm Fe/H}$ -dependent wind mass loss appears to be the main driver of metallicity effects on the evolution of massive stars (including in binaries/multiples). In binaries, composition-dependent radius evolution is another key factor, as it shifts when (and if) Rochelobe overflow occurs, altering the mode, stability, and outcome of mass transfer (e.g. sec 2 in Costa et al. 2024, and references therein). Radii of massive stars are uncertain, but their sensitivity to metallicity is mostly due to changes in opacity and, to a lesser extent, nuclear burning efficiency (Xin et al. 2022). In the absence of self-consistent massive star/binary models with nonsolar abundance patterns representative of the considered environments, $Z_{\rm Fe/H}$ provides a practical scaling of their metallicity dependence. Conversely, relying on $Z_{\rm O/H}$ (or α -elements) leads to largest errors.

7.3. Galaxy/stellar population spectra and diagnostics

Models with non-solar and solar -scaled abundances differ in their predictions for both stellar evolution (isochrones, evolutionary tracks) and atmospheres. In models of old popula-

tions (which formed when <[O/Fe]>_{SFRD} was high, e.g. ellipticals, GCs), the key differences lie in colors, particularly for turnoff/subgiant brach stars used as age indicators, leading to biased age determinations if ignored (e.g. Trager et al. 2000; Thomas & Maraston 2003; Vazdekis et al. 2015; Coelho 2014; Pietrinferni et al. 2021; Knowles et al. 2023; Park et al. 2024). Large grids of α -enhanced evolutionary models of (very) massive stars, which provide the basis for self-consistent SPS models suitable for interpreting young, highly star-forming environments typical of high-z galaxies, have only recently begun to appear in the literature (Grasha et al. 2021; Byrne et al. 2022, 2025). In massive-star dominated populations, the key differences lie in the UV continuum, ionizing outputs, and UV wind features. These are primarily driven by $Z_{\text{Fe/H}}$ rather than nonsolar [O/Fe] per se (see sec 7.2). In general, a young stellar population at lower Z_{Fe/H} is more UV-bright and produces a harder ionising spectrum (e.g. Leitherer et al. 1999; Smith et al. 2002; Stanway et al. 2016; Stanway & Eldridge 2018). Using $Z_{O/H}$ as a proxy for Z_{Fe/H} when deriving SFR with common UV diagnostics (e.g. Bicker & Fritze-v. Alvensleben 2005; Hao et al. 2011; Kennicutt & Evans 2012; Madau & Dickinson 2014) would lead to an overestimation in environments with [O/Fe]>0. Furthermore, ignoring the fact that in such environments iron-poor stars are ionizing relatively oxygen-rich nebulae can lead to misinterpretation of stellar and nebular diagnostics (e.g. Steidel et al. 2016; Trainor et al. 2016; Strom et al. 2017). As gas cooling and heating are determined by $Z_{\rm O/H}$ and $Z_{\rm Fe/H}$, respectively, this can be effectively accounted for in the models by adopting different metallicities for the stellar and gas components (Strom et al. 2018; Sanders et al. 2020; Runco et al. 2021; Strom et al. 2022).

7.4. Transients and phenomena linked to metal-poor progenitors

The uncertainty and difference between $Z_{Fe/H}$ and $Z_{O/H}$ dependent cSFH is the largest in the metal-poor regime. This is also where many transients of stellar-origin appear more common and/or more luminous. These include X-ray sources (Kovlakas et al. 2020; Fornasini et al. 2020; Lehmer et al. 2021), LGRBs and hydrogen-poor superluminous supernovae (Lunnan et al. 2014; Schulze et al. 2018) or luminous fast blue optical transients (Coppejans et al. 2020; Chrimes et al. 2024b,a; Klencki & Metzger 2025). Phenomena theorized to prefer metalpoor progenitors also include stellar BH mergers (Belczynski et al. 2010b; Belczynski et al. 2016; Klencki et al. 2018; Giacobbo et al. 2018; Chruslinska et al. 2019; Neijssel et al. 2019; Broekgaarden et al. 2022; Iorio et al. 2023; Chruślińska et al. 2024a), pair-instability supernovae (Woosley et al. 2002; Stevenson et al. 2019; Sabhahit et al. 2023), and chemically homogeneous evolution (Yoon & Langer 2005; Yoon et al. 2006; Szécsi et al. 2015; Marchant et al. 2016; Mandel & de Mink 2016). Stellar BHs with masses $\gtrsim 30M_{\odot}$, which are found in a substantial fraction (≥40%) BH merger events detected with GW (LIGO Scientific Collaboration et al. 2025), may also require subsolar progenitors (Belczynski et al. 2010a; Romagnolo et al. 2023; Vink et al. 2024; Merritt et al. 2025). Furthermore, harder ionising spectra than predicted by existing SPS models are required to explain the emission properties of metal-poor galaxies (Senchyna et al. 2017; Schaerer et al. 2019; Katz et al. 2023; Telford et al. 2023). Overall, it appears that stellar evolution is more likely to produce (more of the) extreme phenomena at lower metallicities. However, the driving factors and the regime in which these can occur remain unclear. As in the above examples, most of the empirical constraints come from stel-

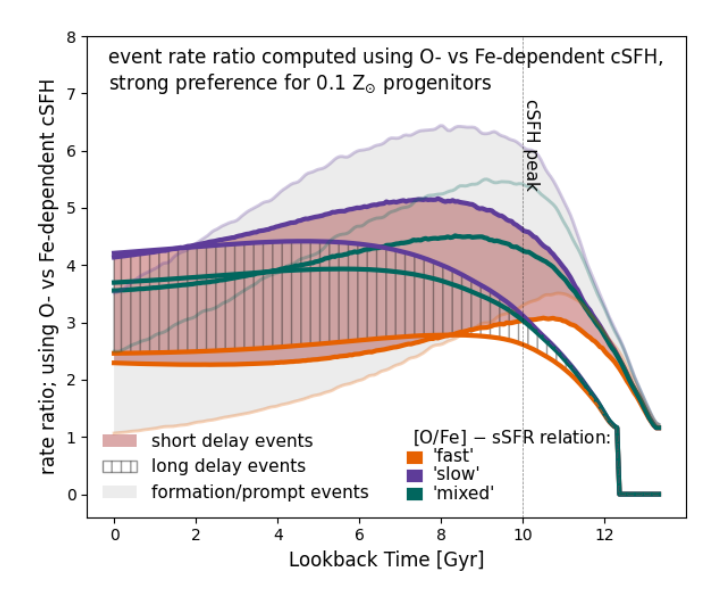


Fig. 9. Relative rate density of events originating from metal-poor progenitors, obtained using $f_{\rm SFR}(Z_{\rm Fe/H},t)$ and $f_{\rm SFR}(Z_{\rm O/H},t)$ as a function of lookback time. Gray area - prompt events/formation rate, brown/hatched area - events with a distribution of delays, peaked at short (10 Myr)/long (1 Gyr) delay times with respect to star formation. Colored lines distinguish assumptions about the [O/Fe]-sSFR relation, other assumptions relevant for the $f_{\rm SFR}(Z_{\rm Fe/H},t)$ and $f_{\rm SFR}(Z_{\rm O/H},t)$ are the same as for the example variation from Sec. 3. Vertical line indicates the time of the peak of the cSFH. Using $f_{\rm SFR}(Z_{\rm O/H},t)$ underestimates metal-poor event rates by a redshift (and model) dependent factor.

lar/transient populations. These require metallicity-dependent cSFH as part of the modelling and interpretation.

In Figure 9 we present a simple estimate of the relative occurrence rate of events with strong preference for low metallicity progenitors calculated using $f_{SFR}(Z_{Fe/H},t)$ and $f_{SFR}(Z_{O/H},t)$. Assuming that in the context of stellar-origin transients and phenomena "metallicity" $\approx Z_{Fe/H}$, this serves to show the bias introduced by the use of metallicity-dependent cSFH based on an incorrect probe. We note that the result shown in Fig. 9 is model-dependent and it should be taken as a *sign and order-of-magnitude* calculation. The event rate $R_{\text{event:X}}$ follows from:

$$R_{\text{event;X}}(t_0) = \int_0^{t_0} \int f_{\text{SFR}}(Z_{X/H}, t') \, \eta(Z_{X/H}) \, p_{\text{delay}}(t_0 - t') \, dZ_{X/H} \, dt'$$
(2)

where index 'X' denotes either oxygen (X=O) or iron (X=Fe). $\eta(Z_{X/H})$ stands for the event progenitor formation efficiency (number per unit stellar mass formed) as a function of metallicity, for which we use a logistic function (used in the context of LGRBs, hydrogen-poor superluminous SNe, BH mergers, c.f. Schulze et al. 2018; Chruślińska et al. 2024a; Disberg et al. 2025):

$$\eta(Z_{X/H}) = \eta_{high} + (\eta_{low} - \eta_{high})/(1. + \exp(-k \cdot (Z_{X/H} - Z_{X/H_{thr}})))$$
 (3)

with k = -10, which leads to a sharp decrease from η_{low} to η_{high} with a midpoint at $Z_{X/H_{thr}}$ and we set this midpoint value to 1/10 of the solar oxygen/iron abundance. We further assume $\eta_{high} = \eta_{low}/100$, i.e. the formation efficiency is not fully truncated at high $Z_{X/H}$ but drops by two orders of magnitude with respect to plateau η_{low} at low $Z_{X/H}$. Since we only compare the relative

rate, η_{low} value is irrelevant. For the delay time distribution, we assume the power-law

$$p_{\text{delay}}(\tau) = \begin{cases} \propto \tau^{-1}, & \tau \ge \tau_{\text{event;min}}, \\ 0, & \tau < \tau_{\text{event;min}}, \end{cases}$$
(4)

normalised to unity between $\tau_{\text{event;min}}$ and Hubble time. This is a conventional approximation for p_{delay} of gravitational wave sources (e.g. BH mergers). We use $\tau_{\text{event;min}}$ =10 Myr and 1 Gyr for events with a "short" (brown region) and "long" delay (hatched region), respectively, for the examples shown in Fig. 9. Both short and long delays are possible for BH mergers within the formation scenarios considered in the literature. Replacing the p_{delay} with a Dirac delta at zero, equation 2 can be used to compute the formation rate/prompt event rate (e.g. LGRB, supernovae). We point out that:

- Using f_{SFR}(Z_{O/H}, t) underestimates metal-poor event rates.
 The difference varies with z/lookback time.
- The difference depends on $f_{\rm SFR}(Z_{Fe/H},t)$ model variation and is the largest for variations with the largest difference between O- and Fe- dependent cSFH (in particular, for 'slow' Fe enrichment model family).
- The difference also depends on p_{delay} (larger for prompt events), $\eta(Z_{X/H})$ (larger for more extreme metallicity thereshold/dependence).
- $f_{SFR}(Z_{Fe/H}, t)$ model variation affects the metal-poor event rate evolution over cosmic time/redshift. In particular, uncertainty in the [O/Fe]-sSFR relation alone affects the evolution, peak location and the magnitude of the rate (factor of 2-3).

Variations in R_{event} due to uncertainty in $f_{\text{SFR}}(Z_{Fe/H}, t)$ across our variations are typically within a factor of a few but can reach $\sim O(10)$ for more extreme $\eta(Z_{Fe/H})$ and p_{delay} choices than used in our example. The bias introduced by the use of $f_{\text{SFR}}(Z_{O/H}, t)$ and uncertainty of the $f_{\text{SFR}}(Z_{Fe/H}, t)$ are both important when considering transients/phenomena sensitive to low metallicity.

8. Conclusions

Oxygen and iron are key to different astrophysical processes, and are primarily produced by nucleosynthetic sources operating on different timescales. Their relative abundance in the interstellar medium varies over time and can significantly depart from the solar ratio. However, observationally, it is often only possible to constrain one of these two elemental abundances, which is then used as a representative proxy for metallicity after being scaled to the solar abundance. Usually, the different roles and evolution of these elements are not distinguished in models and simulations that use a total metal mass fraction to parametrise the effects of metallicity on different processes. In this work, we propose a framework to overcome these observational limitations and provide a more appropriate scaling for the cosmic evolution of the abundances of oxygen and iron that can be used in models. Building on Paper I Ch24, which introduced the theoretical underpinnings of the redshift-invariant [O/Fe]-sSFR relation of galaxies and constrained it empirically, we apply that relation to derive the iron-dependent cosmic star formation history, $f_{SFR}(Z_{Fe/H}, t)$, alongside its oxygen-based counterpart, $f_{SFR}(Z_{O/H}, t)$. Here, we extend and validate the observationbased framework of ChN19; Ch21 against more recent and additional empirical constraints. We also introduce several model variations to bracket the main uncertainties in the core ingredients of our framework, i.e. the distributions of galaxy SFR,

 $Z_{O/H}$, GSMF and [O/Fe]-sSFR relation. This enables us to quantify how these uncertainties propagate to the final result. Notably, the high-z JWST results constrain the evolution of the FMR and MZR at z>3 enough so that it is no longer the dominant source of uncertainty in our $f_{\rm SFR}(Z_{\rm O/H},t)$ estimates. Our main conclusions are the following:

- Star formation with a near-solar [O/Fe] abundance is rare throughout cosmic history; the bulk (at least 70% across our variations) of the integrated stellar mass formed with O/Fe larger than the solar abundance ratio.
- − The SFRD-weighted average metallicity is lower when using [Fe/H] than [O/H] at all redshifts, except when the [O/Fe]–sSFR relation resembles our "fast Fe-enrichment" case, for which \langle [O/Fe] \rangle _{SFRD} may become subsolar at $z \leq 0.4$ (Fig. 4).
- The offset between ⟨[Fe/H]⟩_{SFRD} and ⟨[O/H]⟩_{SFRD} grows to z ≈ 3 and approaches a roughly constant value at higher redshift ([O/Fe]≈0.4-0.5 dex, i.e. up to the CCSN-ratio; Fig. 4). The offset depends primarily on the [O/Fe]–sSFR relation (particularly on the assumed [O/Fe]_{CCSN} for core-collapse supernovae and the minimum delay for enhanced Fe enrichment) and on the galaxy SFR distribution.
- The differences between $f_{SFR}(Z_{O/H}, t)$ and $f_{SFR}(Z_{Fe/H}, t)$ are the largest in the low-metallicity and high-z regimes. These differences are the smallest if the delay in the enhanced Fe enrichment relative to star formation is minimal (our "fast Fe-enrichment" case; Figs. 3 and 7).
- The absorption-derived ⟨[Fe/H]⟩_{HI}(z) from LGRB after-glow–selected sources is broadly consistent with our ⟨[Fe/H]⟩_{SFRD}(z) estimates and is offset from ⟨[O/H]⟩_{SFRD}(z) (Fig. 8). While the current comparison is not constraining for our models, a larger sample (particularly at z > 4) could provide the most direct tests of our f_{SFR}(Z_{Fe/H}, t) framework.

These results underscore that "metallicity" estimates based on oxygen (or α -elements in general) and iron-group probes are not interchangeable. Failing to account for non-solar abundance ratios may lead to important biases and systematic errors. In particular, in environments with [O/Fe] > 0:

- Relying on solar abundance scaling would slightly overpredict O-scaled effects (e.g. gas cooling) and underpredict Fescaled effects (e.g. stellar feedback; by up to a factor of ~ 3).
- Using Z_{O/H} as a solar-scaled proxy for Z_{Fe/H} overestimates hot-star/VMS wind mass loss effects. This non-trivially affects the evolution of stars/multiples, UV and ionising stellar spectra (SFR and metallicity diagnostics), properties of stellar BHs and transients of massive-star origin.
- Using $f_{SFR}(Z_{O/H}, t)$ instead of $f_{SFR}(Z_{Fe/H}, t)$ underestimates the rates of events and phenomena linked to metal-poor progenitors (e.g. LGRBs, stellar BH mergers) by a z-dependent factor, complicating the interpretation of z-trends in their population properties (Fig. 9).

The magnitude of these effects is model-dependent. Our results can be used within specific frameworks to alleviate and quantify these biases. Finally, we emphasise that we obtain the above results simultaneously predicting that galaxies with MW-like M_* are among the dominant contributors to the cosmic SFRD at $z \lesssim 2$ and can form stars with the Sun's $Z_{\rm O/H}$ and $Z_{\rm Fe/H}$ at solar birth epoch. However, for model variations with long ($\gtrsim 10^8 {\rm yr}$) delays in enhanced Fe enrichment (our "slow Fe-enrichment" case) such stars would not coincide with the MDF peak in MW-like galaxies.

$log_{10}(\Phi_*/Mpc^{-3}dex^{-1})$	$log_{10}(M_{GSMF}/M_{\odot})$	$lpha_{high}$
-2.80	10.77	-1.32
-3.02	10.79	-1.34
-3.39	10.90	-1.37
-4.23	11.15	-1.66
-4.90	11.20	-1.95
-5.60	11.15	-2.25
-5.36	10.70	-2.1
-5.60	10.50	-1.98
-6.00	10.60	-1.98
-6.40	10.43	-1.99
-5.65	9.40	-2.01
	-2.80 -3.02 -3.39 -4.23 -4.90 -5.60 -5.36 -5.60 -6.00 -6.40	-2.80 10.77 -3.02 10.79 -3.39 10.90 -4.23 11.15 -4.90 11.20 -5.60 11.15 -5.36 10.70 -5.60 10.50 -6.00 10.60 -6.40 10.43

Table A.1. Parameters of equation A.1, approximating the high-mass part of the GSMF.

Appendix A: Galaxy Stellar Mass Function

The GSMF was obtained by averaging literature results grouped in several redshift bins, as detailed in ChN19. In addition to those listed in table 1 in ChN19, we include more recent works: Stefanon et al. (2021) (z=5.5-10.5), Hamadouche et al. (2024) (z=0.25-2.25), Navarro-Carrera et al. (2024) (z=3.5-8.5) and Weibel et al. (2024) (z=3.5-9.5). This more than doubles the number of GSMF estimates used at z>7.5, and leads to a more gradual evolution compared to ChN19, where the GSMF shows a sharp drop between z=7-8. At lower z the differences are minor. Following ChN19, we distinguish between the (Schechterlike) high-mass part of the GSMF and a power-law part with a slope $\alpha_{\rm GSMF}$ at low $\log_{10}({\rm M_*}) < \log_{10}({\rm M}_{\rm lim})$. We extrapolate the GSMF down to $M_* = 10^6 M_{\odot}$, where it is essentially unconstrained and $\alpha_{\rm GSMF}$ is one of the main sources of uncertainty in $f_{\rm SFR}({\rm Z},z)$ at $z \gtrsim 4$ (ChN19; Ch21).

We assume $\log_{10}(M_{\rm lim}/{\rm M}_{\odot}) = 7.7 + 0.4z$ at z < 4.5 and $\log_{10}(M_{\rm lim}/{\rm M}_{\odot}) = 9.5$ at $z \ge 4.5$. At $\log_{10}({\rm M}_*) < \log_{10}({\rm M}_{\rm lim})$, the GSMF is described as a power-law with slope $\alpha_{\rm GSMF}(z) = -1.4 - 0.08 \cdot z$, reaching $\alpha_{\rm GSMF} = -2.2$ at z = 10, and is normalised to ensure continuity with with the high mass part. Following ChN19, we contrast this with the variation in which the slope is fixed to $\alpha_{\rm GSMF} = \alpha_{\rm fix} = -1.45$, corresponding to the average literature value between z = 0 and z = 2. This serves to discuss the effect of low M_* extrapolation on our results. The resulting GSMF is shown in the top left panel of fig. 6.

Table A.1 summarizes the parameters of a single Schechter function fits to the (high-mass part of the) GSMF used in this work:

$$\Phi\left(M_{*},z\right) = \ln(10)\,\Phi_{*}\left(\frac{M_{*}}{M_{\rm GSMF}}\right)^{\alpha_{\rm high}+1} \exp\left(-\frac{M_{*}}{M_{\rm GSMF}}\right), \tag{A.1}$$

where
$$\Phi(M_*, z) = \frac{dn_{\text{gal}}}{d\log_{10} M_*}$$

We do not extend our calculations beyond z = 10.5, except for extrapolating the cSFH trends shown in Fig. 6. For this purpose, we assume that at z > 10.5 the high-mass GSMF is fixed and we continue with the z-dependent low-mass end as described above. We warn that such extrapolation would lead to an increase in the SFRD at z > 13.

Appendix B: Starburst sequence

The high-SB scenario from Ch21 is based on the interpolation between the results from Bisigello et al. (2018) and Caputi et al.

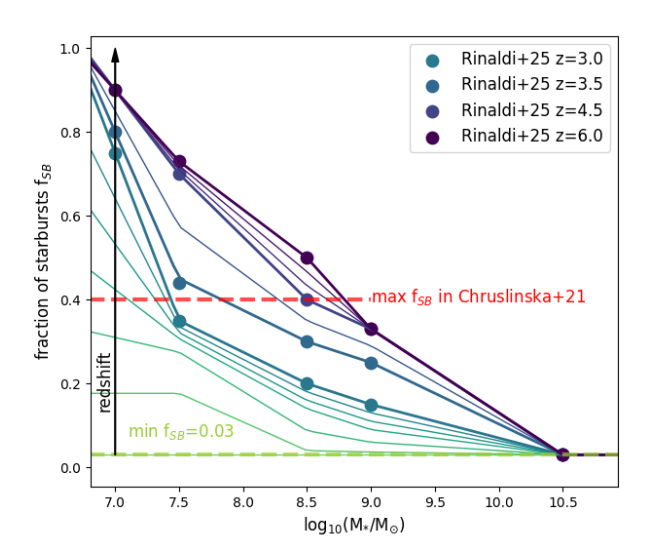


Fig. B.1. Fraction of starbursts as a function of galaxy stellar mass. Lines correspond to redshifts between 0 and 6 with a step of 0.5. For z < 3 and $\log_{10}(M_*/M_{\odot}) > 8$ the dependence is the same as in Ch21, here extended to z > 3 and lower $\log_{10}(M_*)$ following the same approach but using the recent estimates from Rinaldi et al. (2025) (circles, fig. 5 therein).

(2017) and fixed at z > 4.4 (exceeding z of their samples). The resulting f_{SB} increases to low M_* and high z up to f_{SB} =0.4, and the SB sequence is 1 dex above the SMFR. The work of Caputi et al. (2017) has recently been extended to $z \sim 6$ and low $M_* \lesssim 10^7 M_{\odot}$ by Rinaldi et al. (2022, 2025). They report further increase in f_{SB} with z and decreasing M_* , and the lack of a clear distinction between the SB and MS at low $\log_{10}(M_*/M_{\odot})$ <7.5. Rinaldi et al. (2025) suggest that the majority of the cosmic SFRD is produced by the SB galaxies. We modify the $f_{SB}(M_*,$ z) from Ch21 to include the results from Rinaldi et al. (2025) as shown in Fig. B.1 to comment on the impact of such a high SB contribution on our results. However, we assume the SB sequence is 1 dex above the SMFR. This is smaller than the offset between the peaks in the sSFR distribution of SB and MS galaxies in Rinaldi et al. (2025) (see Fig. 3 therein). Additionally, for variations with $a_{SFR} < 1$ (which is the case for Rinaldi et al. 2022, 2025), we require this offset to decrease linearly from 1 dex to 0 dex between $\log_{10}(M_*/M_{\odot})=9$ and $\log_{10}(M_*/M_{\odot})=6$. This is necessary to avoid drastically overestimating the cosmic SFRD(z > 2) (right panel in fig. 6, thick gray lines).

We note that in terms of the results presented in this paper, the high f_{SB} scenario described above would be indistinguishable from a scenario in which the SB sequence is absent and a_{SFR} is z-dependent ($a_{SFR} \sim 0.9$ at z = 0 and becomes $a_{SFR} \lesssim 0.8$ at z > 2).

Appendix C: Overview of model variations

Table C.1 summarizes the variations of assumptions used to describe the statistical properties of the galaxies needed to derive $f_{\rm SFR}(Z_{O/H},t)$ and $f_{\rm SFR}(Z_{Fe/H},t)$ that were considered in this study.

Table C.1. Overview of the assumptions (model variations) considered in this study. Combination of assumptions highlighted in bold corresponds to our example variation.

Variation	Notes				
	[O/Fe] – sSFR relation (following Ch24, see sec. 2.1)				
"fast" Fe enrichment	$f_{\rm la} \propto t^{-1}$, $\tau_{\rm la,min}$ =40 Myr, $m_{e_e}^{CCSN} = 0.03 M_{\odot}$				
"mixed" Fe enrichment	$f_{\rm la}$ following Greggio (2010), ${\rm m}_{CCSN}^{CCSN} = 0.05 M_{\odot}$ $f_{\rm la} \propto t^{-1}$, $\tau_{\rm Ia,min} = 400$ Myr, ${\rm m}_{Fe}^{CCSN} = 0.1 M_{\odot}$				
"slow" Fe enrichment	$f_{\rm la} \propto t^{-1}$, $\tau_{\rm Ia;min} = 400 \; { m Myr}, { m m}_{Fe}^{CCSN} = 0.1 M_{\odot}$				
	SFMR/ galaxy main sequence				
$a_{SFR}=1$	following eq. 15 and table 2 in P23				
$a_{SFR}=0.8$	P23 with shallower slope: parameter a4 in Tab. 2 in P23 set to 0.8				
$a_{SFR}=1 + evol.$	P23 with faster evolution at $z > 1.8$: at $z \ge 1.8$ parameter a1 in Tab. 2 in P23 set to -0.3				
GSMF (following ChN19 with updates, see appendix A)					
$\alpha_{\text{GSMF}}(z)$	low mass end slope steepening with z : $\alpha_{\text{GSMF}} = -1.4 - 0.08 \cdot z$				
$\alpha_{\rm GSMF}$ fixed	α_{GSMF} =-1.45				
	MZR(z = 0) normalisation				
$Z_{\text{O/H;MZR0}} = 9$	fiducial value used here, following Curti et al. (2020) but shifted by +0.2 dex to match recombination line based estimates				
$Z_{O/H;MZR0} = 8.8 - 9.1$	range considered in Ch21, where relevant, we indicate how this would lead to a systematic shift in our results				
	MZR(z=0)				
-	eq. 7 in Ch21 with a_{MZR} =0.28, β_{MZR} =0.23, $M_{0;MZR0}$ = 10.02 to match Curti et al. (2020), $Z_{O/H;MZR0}$ as above				
	FMR(z > 3)				
fixed	redshift-invariant FMR modelled following Ch21				
evol.	evolving normalisation at $z > 3$, parameter $Z_{O/H;0}$ in eq. 1 in Ch21 set to $Z_{O/H;0}(z > 3) = -0.0357$ $(z - 3) + Z_{O/H;MZR0}$				
	contribution of starbursts				
negligible	following Ch21, fixed SB fraction f_{SB} =0.03, SB sequence 0.59 dex above the SFMR				
$high / high f_{SB}$	see appendix B, based on Rinaldi et al. (2025) and considered only with a_{SFR} =1 SFMR variation				

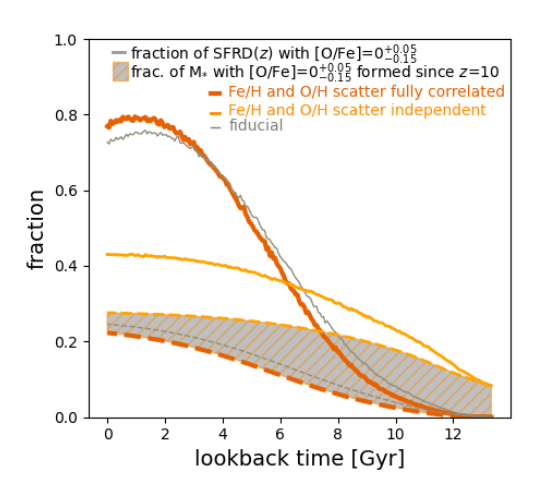


Fig. D.1. Effect of the assumed [O/Fe] scatter (relative to the fiducial case) on the estimated fraction of the SFRD forming with near-solar [O/Fe] (solid lines) and on the cumulative fraction of stellar mass formed with near-solar [O/Fe] since z=10 (dashed lines and gray area). Larger scatter (the fully independent $Z_{\rm O/H}$ and $Z_{\rm Fe/H}$ case) increases these fractions, while smaller scatter (the fully correlated $Z_{\rm O/H}$ and $Z_{\rm Fe/H}$ case) decreases them.

Appendix D: Metallicity spread in galaxies

The SFR within each "galaxy" in our framework is distributed over a range of metallicities. As in ChN19, we model this as a normal distribution centered on the $Z_{\rm O/H}$ assigned to a "galaxy" from the FMR (given its SFR, M_* , and z), with dispersion $\sigma_{\rm VO/H}=0.14$ dex. This is a major simplification, but it does not significantly affect cosmic–volume–averaged results (e.g., metallicity–dependent cosmic SFH). ChN19 motivate this choice with the distribution of H,II–region metallicities in $z\sim0$ disk galaxies from CALIFA (Sánchez-Menguiano et al. 2016, 2017), which is roughly symmetric about the average value at R_e ; we take that average to represent the $Z_{\rm O/H}$ assigned via the scaling relations.

Here we further assume that $Z_{\text{Fe/H}}$ within each "galaxy" follows an analogous normal distribution with the same dispersion, $\sigma_{\text{VFe/H}} = \sigma_{\text{VO/H}}$, centered on the value set by the [O/Fe]–sSFR relation. This additional simplification is justified by the broadly comparable $Z_{\text{O/H}}$ and $Z_{\text{Fe/H}}$ gradients observed in galaxies (Hernandez et al. 2021).

One must still specify the spread in [O/Fe], $\sigma_{\text{VO/Fe}}$. If $Z_{\text{O/H}}$ and $Z_{\text{Fe/H}}$ were fully correlated, then $\sigma_{\text{VO/Fe}} = 0$ and, at a given z, all of the SFR within a "galaxy" would share a single [O/Fe]. If instead the two were independent (e.g., in a highly turbulent ISM mixing), then [O/Fe] would follow a normal distribution with $\sigma_{\text{VO/Fe}} = \sqrt{2}, \sigma_{\text{VO/H}}$. Reality likely lies between these limits; for example, MW stars at fixed age, location, and [Fe/H] show a moderate spread in [O/H]. As our fiducial choice we adopt a weakly uncorrelated case, $\sigma_{\text{VO/Fe}} = \sigma_{\text{VO/H}}/4$. This choice is arbitrary, but it affects only $f_{\text{SFR}}(\text{[O/Fe]},t)$ (Fig. 4, Fig. G.2, Fig. G.3).

Figure D.1 illustrates the impact of $\sigma_{\text{VO/Fe}}$ on the fraction of the cosmic SFRD and the integrated stellar mass formed with near-solar [O/Fe] (as in the top panel of Fig. 4). In general, larger $\sigma_{\text{VO/Fe}}$ broadens the [O/Fe] distribution of the SFRD at each z, increasing the fraction of mass formed with near-solar [O/Fe] and yielding a milder evolution of the instantaneous near-solar SFRD fraction over cosmic time. We show this only for the model variation that maximizes the near-solar [O/Fe] fraction, providing a conservative upper bound on the fraction of mass formed with near-solar [O/Fe] of < 30%. Thus, the specific treatment of scatter does not affect our main conclusion that star formation with near-solar [O/Fe] is rare.

Appendix E: LGRB hosts: HI-weighted mean metallicity in redshift bins

Appendix F: $Z_{O/H}$ and $Z_{Fe/H}$ metallicity distribution functions

In this section we compare the $f_{SFR}(Z_{Fe/H}, z)$ and $f_{SFR}(Z_{O/H}, z)$ integrated over z - i.e. the $Z_{Fe/H}$ - and $Z_{O/H}$ -metallicity distribution functions (MDFs). Figure F.1 shows the MDFs of stars

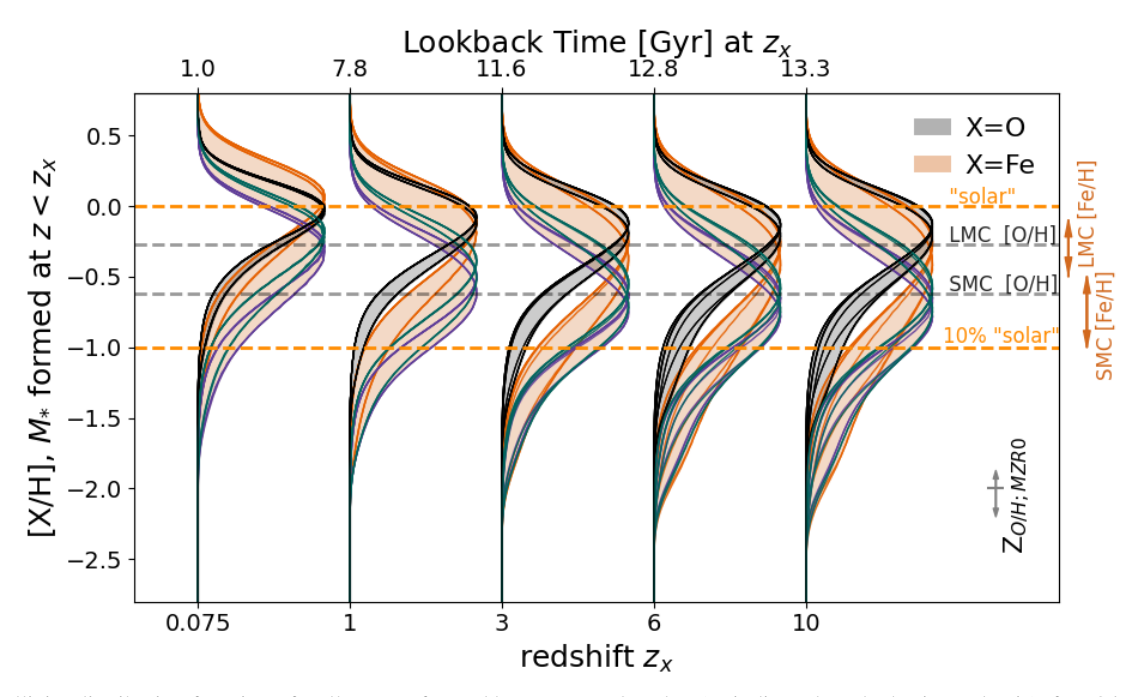


Fig. F.1. Metallicity distribution function of stellar mass formed between z=0 and z_x (as indicated on the horizontal axis), for [O/H] (gray bands, black curves) and [Fe/H] (brown bands, colored curves; colors distinguish the [O/Fe]–sSFR relation as in Fig. 1). Bands show the range spanned by individual model variations, which are shown as lines. Dashed horizontal lines mark solar, 0.1 solar, and LMC/SMC [O/H] (Grevesse & Sauval 1998 reference scale); LMC/SMC [Fe/H] are marked as arrows. Grey arrows indicate the systematic uncertainty (not accounted for in the plotted ranges) from the $Z_{O/H}$ calibration, which shifts all curves by a constant factor. All MDFs are normalised to unity to compare the shapes.

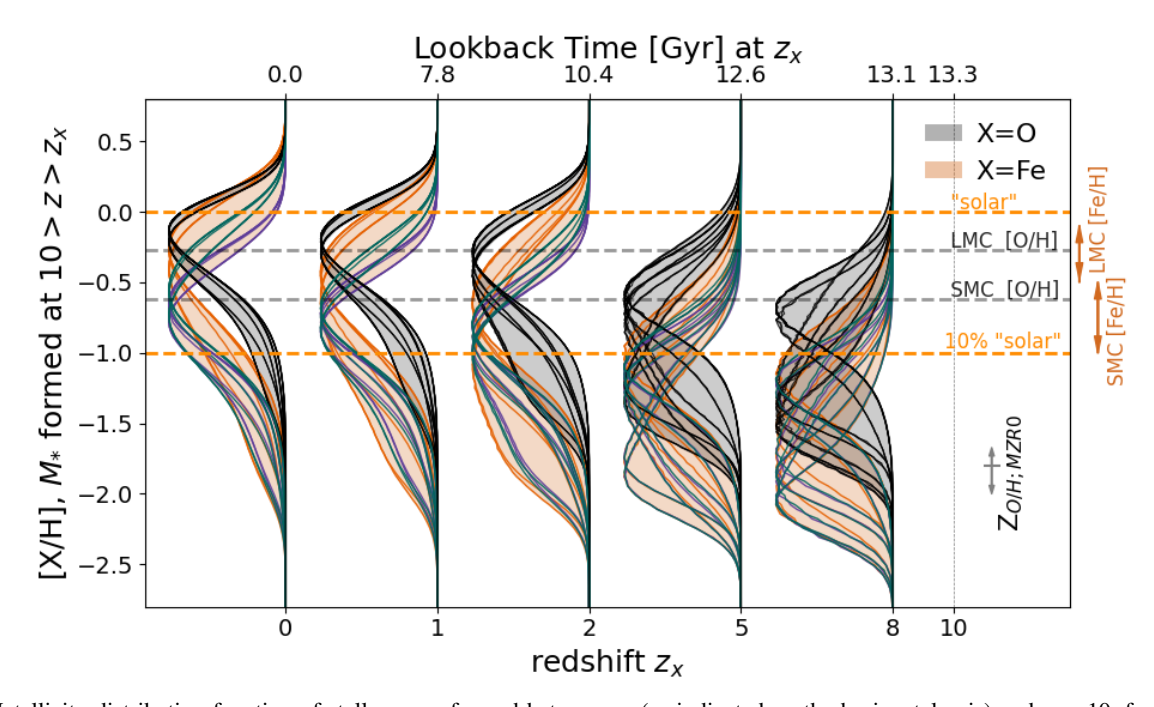


Fig. F.2. Metallicity distribution function of stellar mass formed between z_x (as indicated on the horizontal axis) and z = 10, for [O/H] (gray bands, black curves) and [Fe/H] (brown bands, colored curves; colors distinguish the [O/Fe]–sSFR relation as in Fig. 1). Bands show the range spanned by individual model variations, which are shown as lines. Dashed horizontal lines mark solar, 0.1 solar, and LMC/SMC [O/H] (reference scale (Grevesse & Sauval 1998)); LMC/SMC [Fe/H] are marked as arrows. Gray arrows indicate systematic shifts from $Z_{O/H}$ calibration.

formed between z=0 and increasing z_x : the leftmost curves correspond to stars formed in the last ~ 1 Gyr, while the rightmost curves encompass the full ≈ 13.3 Gyr of cosmic history. For comparison, Fig. F.2 presents the complementary case, showing MDFs of stars formed between z=10 and decreasing z_x , i.e. focusing on the early Universe. Together, these figures il-

lustrate the buildup of the cosmic MDF, with the peak established at $z \leq 3$, where most of the cosmic stellar mass forms, and the low-metallicity tail developed at $z \geq 2$ (cf. Fig. F.2). The brown/black ranges in Fig. F.1 span between the model variations and broaden with increasing z_x , reflecting the fact that our estimates are more uncertain at high z. As before, different as-

selected subsample for which $[M/H]_{tot} \approx [Fe/H]$					
z_{low}	Z_{high}	number in bin	$\langle [\text{Fe/H}] \rangle_{\text{HI}}$	dispersion	
1.7	2.1	6	-0.65	0.38	
2.1	2.5	6	-1.01	0.46	
2.5	2.95	5	-1.2	0.51	
2.95	6.4	5	-1.69	0.23	
all LGRBs					
		all LGR	CBS		
z_{low}	$z_{ m high}$	number in bin	αΒs ⟨[M/H]⟩ _{HI}	dispersion	
$\frac{z_{\text{low}}}{1.7}$	$\frac{z_{\mathrm{high}}}{2.2}$			dispersion 0.64	
		number in bin	$\langle [M/H] \rangle_{HI}$		
1.7	2.2	number in bin	$\langle [\text{M/H}] \rangle_{\text{HI}}$ -0.72	0.64	

Table E.1. $N_{\rm HI}$ -weighted mean metallicity with z based on absorption-derived LGRB host properties as shown in Fig. 8 and described in Section 3.1.3. Redshift bin edges (column 1 and 2) were selected to ensure that each bin contains a similar number of LGRB hosts. Top rows: subsample with dust corrections derived from Zn or accounting for α-enhancement for which $[M/H]_{tot} \approx [Fe/H]$. Bottom rows: also including objects with more approximate dust correction based on α-elements, in which case $[M/H]_{tot}$ may overestimate [Fe/H].

sumptions about the [O/Fe]-sSFR relation (which affect only the Z_{Fe/H}-MDFs) are distinguished by color. For stars formed in the last ~ 1 Gyr, this assumption shifts the peak of the $Z_{\rm Fe/H}$ -MDF to higher (orange lines, 'fast' Fe enrichment) or lower (green/purple lines, 'mixed'/'slow' Fe enrichment) metallicities relative to solar and to the $Z_{O/H}$ -MDF peak. The offset between the peaks reaches up to ~0.3 dex for MDFs integrated over the past 1 Gyr and up to ≥ 0.5 dex when integrating over the full z range spanned by our models (with 'slow' Fe enrichment maximizing the difference). For any fixed variation, the $Z_{\text{Fe/H}}$ -MDF is broader than the corresponding $Z_{O/H}$ -MDF. Aside from the impact of the [O/Fe]-sSFR relation (i.e., comparing curves of the same color), differences appear mainly in the low-metallicity tails. This regime is dominated by contributions from low- M_* galaxies, where the associated uncertainties (parametrized by $a_{\rm SFR}$ and $\alpha_{\rm GSMF}$) accumulate in our model. We caution that all MDFs in Figs. F.2 and F.1 are normalized to unity to facilitate comparison of their shapes, but the total stellar mass formed differs across models (see Sec. 5.2). In particular, variations producing more extended low-metallicity tails generally also yield higher SFRDs (by a factor of $\sim 2-3$ at z < 2, and increasing to higher z), due to the larger contribution of low- M_* galaxies.

Appendix G: Additional figures

Figures G.1 and G.2 show the $f_{SFR}([O/H], z)$ and $f_{SFR}([O/Fe], t)$ distributions for our example variation, respectively. Figure G.3 shows the $f_{SFR}([O/Fe], t)$ for the same variation but assuming a [O/Fe]-sSFR relation corresponding to our "fast Fe enrichment" case. Figure F.2 shows the MDF of stellar mass formed between decreasing z thresholds and z=10, i.e. complementary to Fig. F.1.

Acknowledgements. MCh would like to thank T. Matsuno and J. Klencki for their insightful comments, and K. Heintz for the discussion on the LGRB sample.

Software: matplotlib (Hunter 2007), scipy (Virtanen et al. 2020), numpy (Harris et al. 2020), astropy (Astropy Collaboration et al. 2013; Collaboration et al. 2018).

Data and code availability: data generated during this study and code underlying our analysis will be made publicly available upon the acceptance of this manuscript.

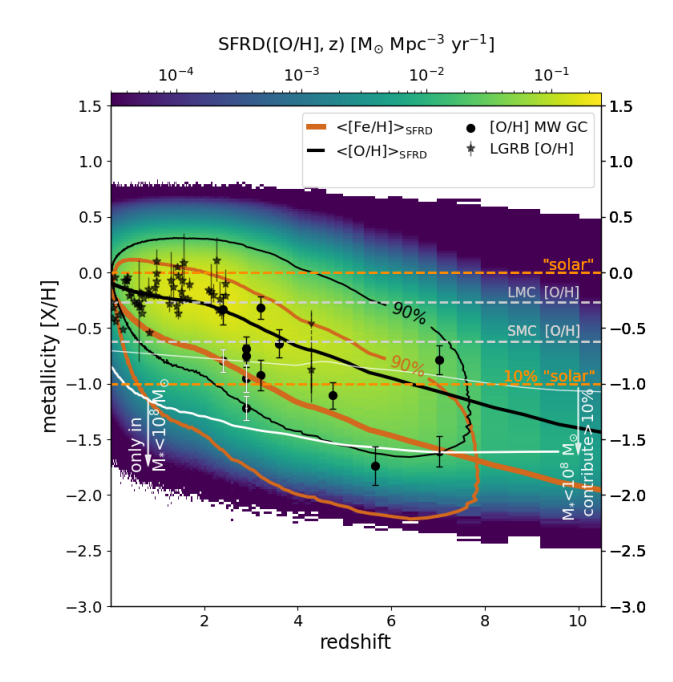


Fig. G.1. Distribution of the cosmic SFRD at different [O/H] and z (color scale), shown for our example variation. Black/brown lines: SFRD-weighted average [O/H] / [Fe/H] at each z. White solid lines: [O/H] below which $M_* < 10^8 M_{\odot}$ galaxies contribute at least 10% of the SFRD (thin line) and below which contribution of $M_* > 10^8 M_{\odot}$ galaxies is negligible (thick line). Stars: [O/H] of individual LGRB hosts (Graham et al. 2023). Dots: [O/H] of MW globular clusters. [O/H] of the LMC and SMC on our solar scale are indicated for the reference.

References

Adamo, A., Hollyhead, K., Messa, M., et al. 2020a, MNRAS, 499, 3267 Adamo, A., Zeidler, P., Kruijssen, J. M. D., et al. 2020b, Space Sci. Rev., 216,

Algera, H. S. B., Inami, H., Oesch, P. A., et al. 2023, MNRAS, 518, 6142 Amarsi, A. M., Nissen, P. E., & Skúladóttir, Á. 2019, A&A, 630, A104 Andrews, B. H. & Martini, P. 2013, ApJ, 765, 140

Arellano-Córdova, K. Z., Esteban, C., García-Rojas, J., & Méndez-Delgado, J. E. 2020, MNRAS, 496, 1051

Asplund, M., Amarsi, A. M., & Grevesse, N. 2021, A&A, 653, A141 Asplund, M., Grevesse, N., Sauval, A. J., & Scott, P. 2009, ARA&A, 47, 481 Astropy Collaboration, Robitaille, T. P., Tollerud, E. J., et al. 2013, A&A, 558, A33

Baldry, I. K., Driver, S. P., Loveday, J., et al. 2012, MNRAS, 421, 621 Belczynski, K., Bulik, T., Fryer, C. L., et al. 2010a, The Astrophysical Journal,

Belczynski, K., Dominik, M., Bulik, T., et al. 2010b, The Astrophysical Journal Letters, 715, L138

Belczynski, K., Holz, D. E., Bulik, T., & O'Shaughnessy, R. 2016, Nature, 534, 512

Bellazzini, M., Muraveva, T., & Garofalo, A. 2025, arXiv e-prints, arXiv:2503.04925

Belokurov, V. & Kravtsov, A. 2024, MNRAS, 528, 3198

Berger, E., Penprase, B. E., Cenko, S. B., et al. 2006, ApJ, 642, 979 Bezanson, R., Labbe, I., Whitaker, K. E., et al. 2024, ApJ, 974, 92

Bian, F., Kewley, L. J., & Dopita, M. A. 2018, ApJ, 859, 175

Bicker, J. & Fritze-v. Alvensleben, U. 2005, Astronomy & Astrophysics, 443, L19

Bisigello, L., Caputi, K. I., Grogin, N., & Koekemoer, A. 2018, A&A, 609, A82 Björklund, R., Sundqvist, J. O., Singh, S. M., Puls, J., & Najarro, F. 2023, A&A, 676, A109

Boco, L., Lapi, A., Chruslinska, M., et al. 2021, ApJ, 907, 110 Boogaard, L. A., Brinchmann, J., Bouché, N., et al. 2018, A&A, 619, A27 Bresolin, F., Kudritzki, R.-P., & Urbaneja, M. A. 2022, ApJ, 940, 32 Bresolin, F., Kudritzki, R.-P., Urbaneja, M. A., et al. 2016, ApJ, 830, 64 Briel, M. M., Fragos, T., Salafia, O. S., et al. 2025, A&A, 701, A84 Brinchmann, J., Charlot, S., White, S. D. M., et al. 2004, MNRAS, 351, 1151 Broekgaarden, F. S., Berger, E., Stevenson, S., et al. 2022, MNRAS, 516, 5737 Bromm, V. & Loeb, A. 2003, Nature, 425, 812 Bromm, V. & Loeb, A. 2003, Nature, 425, 812

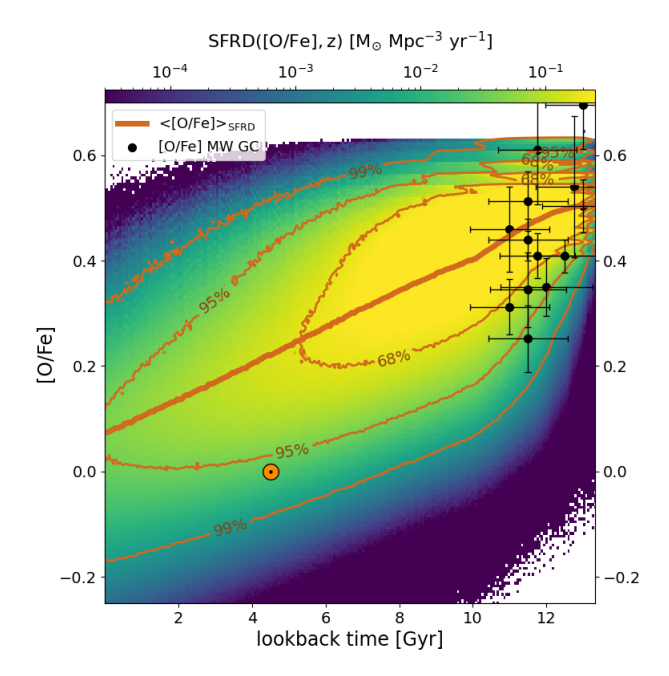


Fig. G.2. Distribution of the cosmic SFRD at different [O/Fe] and lookback time (color scale), shown for our example variation, in particular, assuming the [O/Fe]-sSFR relation corresponding to our "mixed Fe enrichment" case. Brown line: SFRD-weighted average [O/Fe] at each z. Contours enclose 68%, 95% and 99% of the SFRD. Black dots: [O/Fe] of MW globular clusters. Orange dot marks the Sun's formation epoch at [O/Fe]=0.

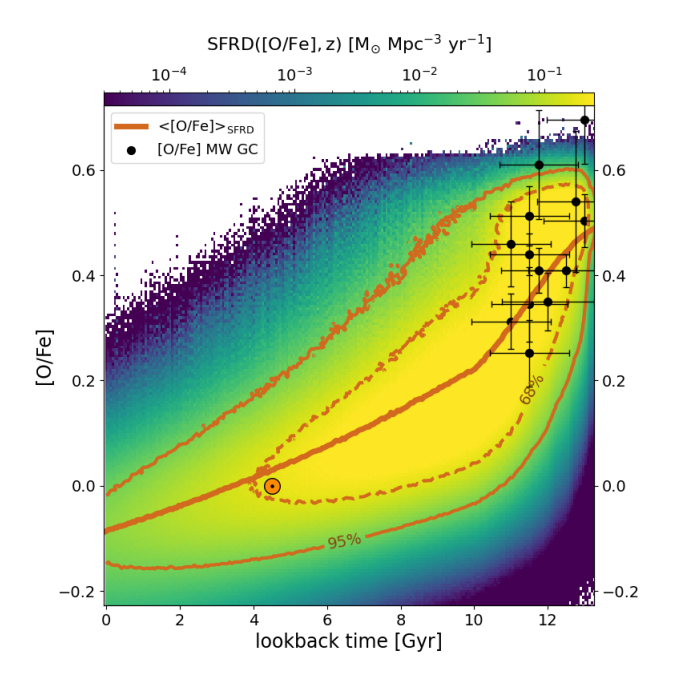


Fig. G.3. Same as Fig. G.3, but assuming the [O/Fe]-sSFR relation corresponding to our "fast Fe enrichment" case.

Buder, S., Sharma, S., Kos, J., et al. 2021a, MNRAS, 506, 150 Buder, S., Sharma, S., Kos, J., et al. 2021b, MNRAS, 506, 150 Bunker, A. J., Saxena, A., Cameron, A. J., et al. 2023, A&A, 677, A88 Byrne, C. M., Eldridge, J. J., & Stanway, E. R. 2025, MNRAS, 537, 2433 Byrne, C. M., Stanway, E. R., Eldridge, J. J., McSwiney, L., & Townsend, O. T. 2022, MNRAS, 512, 5329

Caputi, K. I., Deshmukh, S., Ashby, M. L. N., et al. 2017, ApJ, 849, 45 Carretta, E., Bragaglia, A., Gratton, R., & Lucatello, S. 2009, A&A, 505, 139 Casagrande, L., Schönrich, R., Asplund, M., et al. 2011, A&A, 530, A138 Casey, C. M., Zavala, J. A., Spilker, J., et al. 2018, ApJ, 862, 77

Catelan, M. 2004, in Astronomical Society of the Pacific Conference Series, Vol. 310, IAU Colloq. 193: Variable Stars in the Local Group, ed. D. W. Kurtz & K. R. Pollard, 113

Catelan, M. 2009, Ap&SS, 320, 261

Chemerynska, I., Atek, H., Dayal, P., et al. 2024, arXiv e-prints, arXiv:2407.17110

Chrimes, A. A., Coppejans, D. L., Jonker, P. G., et al. 2024a, A&A, 691, A329

Chrimes, A. A., Jonker, P. G., Levan, A. J., et al. 2024b, MNRAS, 527, L47 Chrimes, A. A., Stanway, E. R., & Eldridge, J. J. 2020, MNRAS, 491, 3479

Christensen, L., Hjorth, J., & Gorosabel, J. 2004, A&A, 425, 913

Chruślińska, M. & Nelemans, G. 2019, MNRAS, 488, 5300

Chruslinska, M., Nelemans, G., & Belczynski, K. 2019, MNRAS, 482, 5012

Chruślińska, M., Nelemans, G., Boco, L., & Lapi, A. 2021, MNRAS, 508, 4994 Chruślińska, M., Pakmor, R., Matthee, J., & Matsuno, T. 2024a, A&A, 686, A186

Chruślińska, M., Pakmor, R., Matthee, J., & Matsuno, T. 2024b, A&A, 686, A186

Clementini, G., Ripepi, V., Garofalo, A., et al. 2023, A&A, 674, A18 Coelho, P. R. T. 2014, MNRAS, 440, 1027

Collaboration, T. A., Price-Whelan, A. M., Sipőcz, B. M., et al. 2018, The As-

tronomical Journal, 156, 123 Coppejans, D. L., Margutti, R., Terreran, G., et al. 2020, ApJ, 895, L23

Costa, G., Chrušlińska, M., Klencki, J., et al. 2024, in Black Holes in the Era of Gravitational-Wave Astronomy, ed. M. Arca Sedda, E. Bortolas, & M. Spera,

Costa, G., Shepherd, K. G., Bressan, A., et al. 2025, Astronomy & Astrophysics, 694, A193

Cresci, G., Mannucci, F., & Curti, M. 2019, A&A, 627, A42

Cullen, F., Shapley, A. E., McLure, R. J., et al. 2021, MNRAS, 505, 903

Curti, M., Cresci, G., Mannucci, F., et al. 2017, MNRAS, 465, 1384

Curti, M., D'Eugenio, F., Carniani, S., et al. 2023, MNRAS, 518, 425

Curti, M., Maiolino, R., Curtis-Lake, E., et al. 2024, A&A, 684, A75 Curti, M., Mannucci, F., Cresci, G., & Maiolino, R. 2020, MNRAS, 491, 944

Davé, R., Finlator, K., & Oppenheimer, B. D. 2011, MNRAS, 416, 1354

De Cia, A., Ledoux, C., Mattsson, L., et al. 2016, A&A, 596, A97

De Cia, A., Ledoux, C., Petitjean, P., & Savaglio, S. 2018, A&A, 611, A76

De Cia, A., Roman-Duval, J., Konstantopoulou, C., et al. 2024, A&A, 683, A216 De Rossi, M. E., Bower, R. G., Font, A. S., Schaye, J., & Theuns, T. 2017, MNRAS, 472, 3354

Di Cesare, C., Matthee, J., Naidu, R. P., et al. 2025, arXiv e-prints, arXiv:2510.19044

Disberg, P., Lankreijer, A., Chruślińska, M., et al. 2025, arXiv e-prints, arXiv:2510.16307

Donnan, C. T., McLure, R. J., Dunlop, J. S., et al. 2024, MNRAS, 533, 3222 Eldridge, J. J. & Stanway, E. R. 2022, Annual Review of Astronomy and Astrophysics, 60, 455

Ellison, S. L., Patton, D. R., Simard, L., & McConnachie, A. W. 2008, ApJ, 672, L107

Feuillet, D. K., Frankel, N., Lind, K., et al. 2019, MNRAS, 489, 1742

Finkelstein, S. L., Bagley, M. B., Ferguson, H. C., et al. 2023, ApJ, 946, L13

Fornasini, F. M., Civano, F., & Suh, H. 2020, MNRAS, 495, 771 Fruchter, A. S., Levan, A. J., Strolger, L., et al. 2006, Nature, 441, 463

Galama, T. J., Vreeswijk, P. M., Van Paradijs, J., et al. 1998, Nature, 395, 670

Gallazzi, A., Charlot, S., Brinchmann, J., White, S. D. M., & Tremonti, C. A. 2005, MNRAS, 362, 41

Garcia, A. M., Torrey, P., Ellison, S. L., et al. 2024, arXiv e-prints, arXiv:2407.06254

Garcia, M., Evans, C. J., Bestenlehner, J. M., et al. 2021, Experimental Astronomy, 51, 887

Giacobbo, N., Mapelli, M., & Spera, M. 2018, MNRAS, 474, 2959

Goswami, S., Silva, L., Bressan, A., et al. 2022, A&A, 663, A1

Götberg, Y., de Mink, S. E., Groh, J. H., Leitherer, C., & Norman, C. 2019, A&A, 629, A134

Götberg, Y., de Mink, S. E., McQuinn, M., et al. 2020, A&A, 634, A134

Gräfener, G. & Hamann, W. R. 2008, A&A, 482, 945

Graham, J. F., Schady, P., & Fruchter, A. S. 2023, ApJ, 954, 13

Grasha, K., Roy, A., Sutherland, R. S., & Kewley, L. J. 2021, ApJ, 908, 241 Greggio, L. 2005, A&A, 441, 1055

Greggio, L. 2010, MNRAS, 406, 22

Grevesse, N. & Sauval, A. J. 1998, Space Sci. Rev., 85, 161

Grudić, M. Y., Kruijssen, J. M. D., Faucher-Giguère, C.-A., et al. 2021, MNRAS, 506, 3239

Gruppioni, C., Béthermin, M., Loiacono, F., et al. 2020, A&A, 643, A8 Hamadouche, M. L., McLure, R. J., Carnall, A., et al. 2024, arXiv e-prints,

arXiv:2412.09592 Hao, C.-N., Kennicutt, R. C., J., Johnson, B. D., Calzetti, D., et al. 2011, The

Astrophysical Journal, 741, 124 Harris, C. R., Millman, K. J., van der Walt, S. J., et al. 2020, Nature, 585, 357

Hayden, M. R., Bovy, J., Holtzman, J. A., et al. 2015, ApJ, 808, 132

```
Heger, A., Fryer, C. L., Woosley, S. E., Langer, N., & Hartmann, D. H. 2003,
   ApJ, 591, 288
```

Heger, A., Müller, B., & Mandel, I. 2023, in The Encyclopedia of Cosmology. Set 2: Frontiers in Cosmology. Volume 3: Black Holes, ed. Z. Haiman, 61-

Heintz, K. E., Brammer, G. B., Giménez-Arteaga, C., et al. 2023, Nature Astronomy, 7, 1517

Henry, A., Rafelski, M., Sunnquist, B., et al. 2021, ApJ, 919, 143

Hernandez, S., Aloisi, A., James, B. L., et al. 2021, ApJ, 908, 226

Hinshaw, G., Larson, D., Komatsu, E., et al. 2013, ApJS, 208, 19

Hirschi, R., Meynet, G., & Maeder, A. 2005, A&A, 443, 581

Hjorth, J., Sollerman, J., Møller, P., et al. 2003, Nature, 423, 847

Hunter, J. D. 2007, Computing in Science & Engineering, 9, 90

Iben, I., J. & Tutukov, A. V. 1984, ApJS, 54, 335

Iglesias, C. A. & Rogers, F. J. 1996, ApJ, 464, 943

Inkenhaag, A., Schady, P., Wiseman, P., et al. 2025, MN-RAS[arXiv:2506.08114]

Iorio, G., Mapelli, M., Costa, G., et al. 2023, MNRAS, 524, 426

Janka, H. T., Langanke, K., Marek, A., Martínez-Pinedo, G., & Müller, B. 2007, Phys. Rep., 442, 38

Japelj, J., Vergani, S. D., Salvaterra, R., et al. 2016, A&A, 590, A129 Jenkins, E. B. 2009, ApJ, 700, 1299

Kashino, D., Lilly, S. J., Renzini, A., et al. 2022, ApJ, 925, 82

Kashino, D., Renzini, A., Silverman, J. D., & Daddi, E. 2016, ApJ, 823, L24 Katz, H., Liu, S., Kimm, T., et al. 2022, PRISM: A Non-Equilibrium, Multi-

phase Interstellar Medium Model for Radiation Hydrodynamics Simulations of Galaxies

Katz, H., Saxena, A., Cameron, A. J., et al. 2023, MNRAS, 518, 592

Kennicutt, Robert C., J. & Evans, Neal J., I. 2012, Annual Review of Astronomy and Astrophysics, 50, 531

Kewley, L. J. & Ellison, S. L. 2008, ApJ, 681, 1183 Kewley, L. J., Nicholls, D. C., & Sutherland, R. S. 2019, ARA&A, 57, 511

Khusanova, Y., Bethermin, M., Le Fèvre, O., et al. 2021, A&A, 649, A152 Kippenhahn, R., Weigert, A., & Weiss, A. 2012, Stellar Structure and Evolution, 2nd edn. (Springer)

Klencki, J. & Metzger, B. D. 2025, arXiv e-prints, arXiv:2510.09745 Klencki, J., Moe, M., Gladysz, W., et al. 2018, A&A, 619, A77

Knowles, A. T., Sansom, A. E., Vazdekis, A., & Allende Prieto, C. 2023, MN-RAS, 523, 3450

Kobayashi, C., Leung, S.-C., & Nomoto, K. 2020, ApJ, 895, 138

Kobayashi, C. & Taylor, P. 2023, arXiv e-prints, arXiv:2302.07255

Konstantopoulou, C., De Cia, A., Krogager, J.-K., et al. 2024, A&A, 691, A129 Kotiwale, G., Matthee, J., Kashino, D., et al. 2025, arXiv e-prints, arXiv:2510.19959

Kovlakas, K., Zezas, A., Andrews, J. J., et al. 2020, Monthly Notices of the Royal Astronomical Society, 498, 4790

Krogager, J.-K., De Cia, A., Heintz, K. E., et al. 2024, MNRAS, 535, 561 Kroupa, P. 2001, MNRAS, 322, 231

Krtička, J. & Kubát, J. 2018, A&A, 612, A20

Kruijssen, J. M. D. 2025, arXiv e-prints, arXiv:2501.16438

Krumholz, M. R., McKee, C. F., & Bland-Hawthorn, J. 2019, ARA&A, 57, 227 Kudritzki, R. P. 2002, ApJ, 577, 389

Lagos, C. d. P., Theuns, T., Schaye, J., et al. 2016, MNRAS, 459, 2632 Langer, N. 2012, ARA&A, 50, 107 Langer, N. & Norman, C. A. 2006, ApJ, 638, L63

Langeroodi, D. & Hjorth, J. 2023, arXiv e-prints, arXiv:2307.06336

Lara-López, M. A., Cepa, J., Bongiovanni, A., et al. 2010, A&A, 521, L53

Laseter, I. H., Maseda, M. V., Bunker, A. J., et al. 2025, arXiv e-prints, arXiv:2510.15024

Laseter, I. H., Maseda, M. V., Curti, M., et al. 2024, A&A, 681, A70

Legnardi, M. V., Milone, A. P., Armillotta, L., et al. 2022, MNRAS, 513, 735 Legnardi, M. V., Milone, A. P., Cordoni, G., et al. 2024, A&A, 687, A160

Lehmer, B. D., Eufrasio, R. T., Basu-Zych, A., et al. 2021, ApJ, 907, 17

Leitherer, C., Schaerer, D., Goldader, J. D., et al. 1999, ApJS, 123, 3 Leja, J., van Dokkum, P. G., Franx, M., & Whitaker, K. E. 2015, ApJ, 798, 115 LIGO Scientific Collaboration, Virgo Collaboration, & KAGRA Collaboration.

2025, arXiv e-prints [arXiv:2508.18082] Livio, M. & Mazzali, P. 2018, Phys. Rep., 736, 1

Lodders, K., Palme, H., & Gail, H. P. 2009, Landolt Börnstein, 4B, 712 Loiacono, F., Decarli, R., Gruppioni, C., et al. 2021, A&A, 646, A76

Lunnan, R., Chornock, R., Berger, E., et al. 2014, ApJ, 787, 138 Madau, P. & Dickinson, M. 2014, ARA&A, 52, 415 Madau, P. & Fragos, T. 2017, ApJ, 840, 39

Maiolino, R. & Mannucci, F. 2019, A&A Rev., 27, 3

Maiolino, R., Nagao, T., Grazian, A., et al. 2008, A&A, 488, 463

Mandel, I. & de Mink, S. E. 2016, Monthly Notices of the Royal Astronomical Society, 458, 2634

Mannucci, F., Cresci, G., Maiolino, R., Marconi, A., & Gnerucci, A. 2010, MN-RAS, 408, 2115

Mannucci, F., Salvaterra, R., & Campisi, M. A. 2011, MNRAS, 414, 1263

Maoz, D. & Mannucci, F. 2012, PASA, 29, 447

Maoz, D., Mannucci, F., & Nelemans, G. 2014, ARA&A, 52, 107

Marchant, P., Langer, N., Podsiadlowski, P., Tauris, T. M., & Moriya, T. J. 2016, Astronomy & Astrophysics, 588, A50

Martins, F., Palacios, A., Schaerer, D., & Marques-Chaves, R. 2025, A&A, 698, A262

Martis, N., Withers, S., Felicioni, G., et al. 2025, arXiv e-prints, arXiv:2503.01579

Massari, D. 2025, Research Notes of the American Astronomical Society, 9, 64 Massari, D., Koppelman, H. H., & Helmi, A. 2019, A&A, 630, L4

Matteucci, F. & Greggio, L. 1986, A&A, 154, 279

McKenzie, M. & Bekki, K. 2021, MNRAS, 507, 834

Mérida, R. M., Pérez-González, P. G., Sánchez-Blázquez, P., et al. 2023, ApJ, 950, 125

Merritt, J., Stevenson, S., Sander, A., et al. 2025, arXiv e-prints, arXiv:2507.17052

Meynet, G., Chomienne, V., Ekström, S., et al. 2015, A&A, 575, A60

Monty, S., Belokurov, V., Sanders, J. L., et al. 2024, MNRAS, 533, 2420

Monty, S., Strom, A. L., Stanton, T. M., et al. 2025, MNRAS, 542, 1443

Monty, S., Yong, D., Marino, A. F., et al. 2023, MNRAS, 518, 965

Morishita, T., Stiavelli, M., Grillo, C., et al. 2024, arXiv e-prints, arXiv:2402.14084

Muraveva, T., Giannetti, A., Clementini, G., Garofalo, A., & Monti, L. 2025, MNRAS, 536, 2749

Muzzin, A., Marchesini, D., Stefanon, M., et al. 2013, ApJ, 777, 18

Nakajima, K., Ouchi, M., Isobe, Y., et al. 2023, arXiv e-prints, arXiv:2301.12825 Nakajima, K., Ouchi, M., Xu, Y., et al. 2022, ApJS, 262, 3

Narloch, W., Pietrzyński, G., Gieren, W., et al. 2021, A&A, 647, A135

Navarro-Carrera, R., Rinaldi, P., Caputi, K. I., et al. 2024, ApJ, 961, 207

Neijssel, C. J., Vigna-Gómez, A., Stevenson, S., et al. 2019, MNRAS, 490, 3740 Nissen, P. E. 2015, A&A, 579, A52 Nomoto, K. 1982, ApJ, 253, 798

Nomoto, K., Iwamoto, K., Nakasato, N., et al. 1997, Nucl. Phys. A, 621, 467 Park, M., Conroy, C., Johnson, B. D., et al. 2024, arXiv e-prints, arXiv:2410.21375

Pauldrach, A. W. A., Feldmeier, A., Puls, J., & Kudritzki, R. P. 1993, Space Sci. Rev., 66, 105

Perley, D. A., Tanvir, N. R., Hjorth, J., et al. 2016, ApJ, 817, 8 Pietrinferni, A., Cassisi, S., Salaris, M., Percival, S. B., & Ferguson, J. W. 2009, The Astrophysical Journal, 697, 275

Pietrinferni, A., Hidalgo, S., Cassisi, S., et al. 2021, ApJ, 908, 102

Popesso, P., Concas, A., Cresci, G., et al. 2023, MNRAS, 519, 1526

Puls, J., Vink, J. S., & Najarro, F. 2008, A&A Rev., 16, 209

Reina-Campos, M., Keller, B. W., Kruijssen, J. M. D., et al. 2022, MNRAS, 517, 3144

Renaud, F. 2018, New A Rev., 81, 1

Revalski, M., Rafelski, M., Henry, A., et al. 2024, ApJ, 966, 228

Richings, A. J., Schaye, J., & Oppenheimer, B. D. 2014, Monthly Notices of the Royal Astronomical Society, 440, 3349–3369

Rinaldi, P., Caputi, K. I., van Mierlo, S. E., et al. 2022, ApJ, 930, 128

Rinaldi, P., Navarro-Carrera, R., Caputi, K. I., et al. 2025, ApJ, 981, 161

Rodighiero, G., Daddi, E., Baronchelli, I., et al. 2011, ApJ, 739, L40

Romagnolo, A., Gormaz-Matamala, A. C., & Belczynski, K. 2023, arXiv e-prints [arXiv:2311.18841]

Romaniello, M., Primas, F., Mottini, M., et al. 2008, A&A, 488, 731

Runco, J. N., Shapley, A. E., Sanders, R. L., et al. 2021, MNRAS, 502, 2600 Sabhahit, G. N., Vink, J. S., Sander, A. A. C., & Higgins, E. R. 2023, MNRAS, 524, 1529

Saccardi, A., Vergani, S. D., De Cia, A., et al. 2023, A&A, 671, A84

Saccardi, A., Vergani, S. D., Izzo, L., et al. 2025, arXiv e-prints, arXiv:2506.04340

Sánchez-Menguiano, L., Sánchez, S. F., Pérez, I., et al. 2017, A&A, 603, A113 Sánchez-Menguiano, L., Sánchez, S. F., Pérez, I., et al. 2016, A&A, 587, A70 Sanders, R. L., Shapley, A. E., Jones, T., et al. 2021, ApJ, 914, 19

Sanders, R. L., Shapley, A. E., Kriek, M., et al. 2018, ApJ, 858, 99 Sanders, R. L., Shapley, A. E., Reddy, N. A., et al. 2020, MNRAS, 491, 1427 Sanders, R. L., Shapley, A. E., Topping, M. W., Reddy, N. A., & Brammer, G. B. 2024, ApJ, 962, 24

Sargent, M. T., Béthermin, M., Daddi, E., & Elbaz, D. 2012, ApJ, 747, L31 Schaerer, D., Fragos, T., & Izotov, Y. I. 2019, Astronomy & Astrophysics, 622,

Schneider, F. R. N., Podsiadlowski, P., & Müller, B. 2021, A&A, 645, A5 Scholte, D., Saintonge, A., Moustakas, J., et al. 2024, MNRAS, 535, 2341

Schreiber, C., Pannella, M., Elbaz, D., et al. 2015, A&A, 575, A74 Schulze, S., Krühler, T., Leloudas, G., et al. 2018, Monthly Notices of the Royal

Astronomical Society, 473, 1258 Senchyna, P., Stark, D. P., Vidal-García, A., et al. 2017, MNRAS, 472, 2608 Sesar, B., Banholzer, S. R., Cohen, J. G., et al. 2014, ApJ, 793, 135

Sharda, P., Amarsi, A. M., Grasha, K., et al. 2023, Monthly Notices of the Royal Astronomical Society, 518, 3985

- Simmonds, C., Tacchella, S., McClymont, W., et al. 2025, arXiv e-prints, arXiv:2508.04410
- Smith, L. J., Norris, R. P. F., & Crowther, P. A. 2002, Monthly Notices of the Royal Astronomical Society, 337, 1309
- Smith, N. 2014, ARA&A, 52, 487
- Speagle, J. S., Steinhardt, C. L., Capak, P. L., & Silverman, J. D. 2014, ApJS, 214, 15
- Spina, L., Ting, Y. S., De Silva, G. M., et al. 2021, MNRAS, 503, 3279
- Stanton, T. M., Cullen, F., McLure, R. J., et al. 2024, arXiv e-prints, arXiv:2405.00774
- Stanway, E. R. & Eldridge, J. J. 2018, MNRAS, 479, 75
- Stanway, E. R., Eldridge, J. J., & Becker, G. D. 2016, Monthly Notices of the Royal Astronomical Society, 456, 485
- Stefanon, M., Bouwens, R. J., Labbé, I., et al. 2021, ApJ, 922, 29
- Steidel, C. C., Strom, A. L., Pettini, M., et al. 2016, ApJ, 826, 159
- Stevenson, S., Sampson, M., Powell, J., et al. 2019, The Astrophysical Journal, 882, 121
- Strom, A. L., Rudie, G. C., Steidel, C. C., & Trainor, R. F. 2022, ApJ, 925, 116
- Strom, A. L., Steidel, C. C., Rudie, G. C., Trainor, R. F., & Pettini, M. 2018, ApJ, 868, 117
- Strom, A. L., Steidel, C. C., Rudie, G. C., et al. 2017, ApJ, 836, 164
- Szécsi, D., Langer, N., Yoon, S.-C., et al. 2015, Astronomy & Astrophysics, 581, A15
- Tanvir, N. R., Fox, D. B., Levan, A. J., et al. 2009, Nature, 461, 1254
- Telford, O. G., Badenes, C., Eldridge, J. J., Stanway, E. R., et al. 2023, The Astrophysical Journal, 943, 65
- Telford, O. G., Dalcanton, J. J., Skillman, E. D., & Conroy, C. 2016, ApJ, 827, 35
- Thomas, D. & Maraston, C. 2003, A&A, 401, 429
- Tinsley, B. M. 1979, ApJ, 229, 1046
- Tomczak, A. R., Quadri, R. F., Tran, K.-V. H., et al. 2016, ApJ, 817, 118
- Topping, M. W., Shapley, A. E., Reddy, N. A., et al. 2020, MNRAS, 495, 4430
- Torrey, P., Vogelsberger, M., Hernquist, L., et al. 2018, MNRAS, 477, L16
- Trager, S. C., Faber, S. M., Worthey, G., & González, J. J. 2000, AJ, 119, 1645
- Trainor, R. F., Strom, A. L., Steidel, C. C., & Rudie, G. C. 2016, ApJ, 832, 171
- Tremonti, C. A., Heckman, T. M., Kauffmann, G., et al. 2004, ApJ, 613, 898
- VandenBerg, D. A., Bergbusch, P. A., Dotter, A., et al. 2012, ApJ, 755, 15
- VandenBerg, D. A., Brogaard, K., Leaman, R., & Casagrande, L. 2013, ApJ, 775, 134
- Vazdekis, A., Coelho, P., Cassisi, S., et al. 2015, MNRAS, 449, 1177
- Vergani, S. D., Salvaterra, R., Japelj, J., et al. 2015, A&A, 581, A102 Vink, J. S. 2022, ARA&A, 60, 203
- Vink, J. S. & de Koter, A. 2005, A&A, 442, 587
- Vink, J. S., de Koter, A., & Lamers, H. J. G. L. M. 2001, A&A, 369, 574
- Vink, J. S., Muijres, L. E., Anthonisse, B., et al. 2011, A&A, 531, A132
- Vink, J. S., Sabhahit, G. N., Higgins, E. R., et al. 2024, Astronomy & Astrophysics, 689, A24, see also arXiv:2407.07204
- Vink, J. S. & Sander, A. A. C. 2021, MNRAS, 504, 2051
- Virtanen, P., Gommers, R., Oliphant, T. E., et al. 2020, Nature Methods, 17, 261
- Vreeswijk, P. M., Ellison, S. L., Ledoux, C., et al. 2004, A&A, 419, 927
- Wang, B. & Han, Z. 2012, New A Rev., 56, 122
- Webbink, R. F. 1984, ApJ, 277, 355
- Weibel, A., Oesch, P. A., Barrufet, L., et al. 2024, MNRAS, 533, 1808
- Wheeler, J. C., Sneden, C., & Truran, Jr., J. W. 1989, ARA&A, 27, 279
- Whitler, L., Stark, D. P., Topping, M. W., et al. 2025, arXiv e-prints, arXiv:2501.00984
- Woosley, S. E. & Heger, A. 2006, ApJ, 637, 914
- Woosley, S. E., Heger, A., & Weaver, T. A. 2002, Reviews of Modern Physics, 74, 1015
- Xin, C., Renzo, M., & Metzger, B. D. 2022, MNRAS, 516, 5816
- Yates, R. M., Kauffmann, G., & Guo, Q. 2012, MNRAS, 422, 215
- Yoon, S. C. & Langer, N. 2005, A&A, 443, 643
- Yoon, S.-C., Langer, N., & Norman, C. 2006, Astronomy & Astrophysics, 460, 199